



Experimental and kinetic study on the solar-driven iron-based chemical looping dry reforming of methane

Hao Zhang^a, Dazhi Yang^{a,*}, Yong Shuai^{b,*}, Xiaomi Zhang^a, Boxi Geng^b, Boshu Jiang^b, Bachirou Guene Lougou^b, Dongmei Han^b, Qinghui Pan^b, Fuqiang Wang^b

^a School of Electrical Engineering and Automation, Harbin Institute of Technology, Harbin, Heilongjiang, China

^b School of Energy Science and Engineering, Harbin Institute of Technology, Harbin, Heilongjiang, China

ARTICLE INFO

Keywords:

Solar thermochemistry
CO₂ splitting
Partial oxidation of methane
Reaction kinetics
Syngas

ABSTRACT

The chemical looping dry reforming of methane (CL-DRM) represents a promising pathway for large-scale engineering applications of thermochemical decarbonization techniques. To elucidate the intricate reaction mechanism of CL-DRM, a comprehensive kinetic model encompassing both gas-phase reactions and ferrite surface reactions is developed in this study. This model can serve as a numerical foundation for tracing the reaction progression of comparable iron-based oxygen carriers, allowing visualization of all reaction pathways and further determination of optimal reaction conditions. Besides, foam-structured materials employing NiO-doped CoFe₂O₄ as oxygen carriers were prepared to conduct application experiments for the CL-DRM on a self-designed solar thermochemical platform. The experimental outcomes, obtained under temperature conditions guided by numerical predictions, validate the promising feasibility of employing Ni-doped ferrite in the CL-DRM reaction system. At a reaction temperature of only 1150 K, remarkable peaks in H₂ yield of 23.5 mL min⁻¹ g⁻¹, CO yield of 11.6 mL min⁻¹ g⁻¹, and CH₄ conversion around 90% are attained, with a net solar-to-fuel conversion efficiency of 1.93%. A comparative analysis conducted with the conventional two-step thermochemical cycle under the same experimental setup underscores the notable advantages of CL-DRM in terms of syngas production capacity and conversion efficiency. Consequently, CL-DRM can be regarded as a pivotal transition towards the realization of a fully carbon-free thermochemical technology.

1. Introduction

Given the pressing energy and environmental challenges, thermochemical decarbonization technology presents a promising approach for large-scale carbon dioxide utilization and resource recycling [1–3]. The fundamental principle involves using thermal energy as the driving force to overcome the reaction energy barrier of the carbon–oxygen double bond, thereby achieving the conversion of thermal energy into chemical energy. By pairing it with concentrating solar power (CSP), which can provide sufficient energy for the thermochemical reaction in a clean and renewable fashion, the resultant system has the potential of further lowering carbon emissions by around 40% and substantially enhancing the fuel's calorific value, thus ultimately yielding considerable economic and environmental benefits [4,5].

At present, there exist four solar thermochemical technologies serving CO₂ resource utilization: (i) solar thermolysis [6], (ii) dry reforming of methane (DRM) [7], (iii) two-step thermochemical cycle (TSTC) [8], and (iv) chemical looping dry reforming of methane (CL-DRM) [9–11]. Among these technologies, solar thermolysis, despite its

simplicity in reaction principle involving the direct splitting of H₂O or CO₂, has hitherto been considered relatively unpromising due to constraints associated with the high-temperature requirements (above 3000°C at atmospheric pressure) and the susceptibility of gas products to recombination [12,13]. Whereas DRM has undergone initial industrialization, the full-scale commercial adoption of this technology has been significantly impeded by the additional economic burdens linked to the separation process of the produced syngas, which comprises a mixture of H₂ and CO [14,15]. In contrast, TSTC divides the oxidation–reduction process into a two-step cycle, thereby facilitating the in-situ separation of H₂ and CO. Additionally, TSTC exclusively utilizes H₂O or CO₂ as feedstock, and in the case of being powered by CSP, it can theoretically achieve total avoidance of CO₂ emission [8]. Nonetheless, the relatively elevated reaction temperature (above 1200°C at atmospheric pressure) presents a substantial challenge to the reaction performance of oxygen carriers. Additionally, the inevitable heat loss associated with the high temperature significantly impacts the ultimate energy conversion efficiency [16–18]. By combining the advantages of

* Corresponding authors.

E-mail addresses: yangdazhi.nus@gmail.com (D. Yang), shuaiyong@hit.edu.cn (Y. Shuai).

<https://doi.org/10.1016/j.cej.2024.154075>

Received 31 March 2024; Received in revised form 30 June 2024; Accepted 16 July 2024

Available online 20 July 2024

1385-8947/© 2024 Elsevier B.V. All rights are reserved, including those for text and data mining, AI training, and similar technologies.

Nomenclature**Abbreviations**

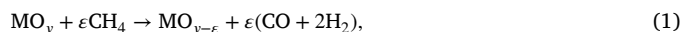
50%CF-Ni	50wt% CoFe ₂ O ₄ -NiO
CL-DRM	Chemical looping dry reforming of methane
CSP	Concentrating solar power
DRGEP	Directed relation graph with error propagation
DRM	Dry reforming of methane
FSM	Foam-structured material
TSTC	Two step thermochemical cycle

Variables

β_i	Temperature exponent
$\eta_{\text{elec-thermal}}$	Electrical-to-thermal efficiency of the solar simulator, %
$\eta_{\text{solar-to-fuel, net}}$	Net solar-to-fuel efficiency, %
$\eta_{\text{solar-to-fuel}}$	Solar-to-fuel efficiency, %
η_{thermal}	Solar-to-thermal efficiency, %
$\nu_{A,i}$	Stoichiometric coefficient of species <i>A</i> in the <i>i</i> th reaction
ω_i	Reaction rate of the <i>i</i> th reaction, mol cm ⁻³ s ⁻¹
ω_k	Production rate of the <i>k</i> th species, mol cm ⁻³ s ⁻¹
ϵ_w	External emissivity of quartz window
A_t	Absolute tolerance
A_i	Pre-exponential factor of the <i>i</i> th reaction
A_s	Heat transfer area of the reactor surface, m ²
A_w	Heat transfer area of the quartz window, m ²
E_{normax}	Maximum normalization error
$E_{a,i}$	Activation energy, cal mol ⁻¹
F^{in}	Flow rate at the inlet of the solar reactor, mL min ⁻¹
F^{out}	Flow rate at the outlet of the solar reactor, mL min ⁻¹
h_s	Free convection heat transfer coefficient, W m ⁻² K ⁻⁴
K_{ci}	Equilibrium constant
k_{fi}	Forward rate constants of the <i>i</i> th reaction
k_{ri}	Reverse rate constants of the <i>i</i> th reaction
P_{elec}	Electrical power of the solar simulator, kW
Q_{conv}	Convection heat loss from the reactor surface, J
Q_{rad}	Radiation heat loss from the quartz window, J
q_i	Rate-of-progress variables for all reactions involving the <i>k</i> th species, mol cm ⁻³ s ⁻¹
r_{CO}	CO yield, mL min ⁻¹
R_t	Relative tolerance
r_A	Immediate errors introduced by the removal of another species <i>B</i> from the mechanism
$R_A(B)$	R-value determining the choice of species
r_{CH_4}	CH ₄ feed rate, mL min ⁻¹
r_{H_2}	H ₂ yield, mL min ⁻¹
T	Temperature, K
T_{reac}	Reaction temperature, K
T_{surf}	Reactor surface temperature, K
ν''_{ki}	Reverse stoichiometric coefficients
ν'_{ki}	Forward stoichiometric coefficients

ν_{ki}	Stoichiometric coefficients
X_m	Values of the target species in the master mechanism
X_s	Values of the target species in the skeletal mechanism
X_k	Molar concentration of the <i>k</i> th species
X_{CH_4}	Conversion of CH ₄ feed gas, %
X_{CO_2}	Conversion of CO ₂ feed gas, %
Constant	
σ	Stefan-Boltzmann constant, $5.67 \times 10^{-8} \text{ W m}^{-2} \text{ K}^{-4}$
HHV _{CO}	High heating value of CO, 12.64 MJ Nm ⁻³
HHV _{CH₄}	High heating value of CH ₄ , 39.82 MJ Nm ⁻³
HHV _{H₂}	High heating value of H ₂ , 12.74 MJ Nm ⁻³
R	Ideal gas constant, 8.314 kJ mol ⁻¹ K ⁻¹
T_0	Environmental temperature, 298.15 K
Indexes	
i	Index for reactions, $i = 1, \dots, I$
k	Index for species, $k = 1, \dots, K$

low reaction temperature requirements and in-situ separation, CL-DRM presents a promising alternative for the cleaner utilization of fossil fuels and the harnessing of CO₂ resources [19–21]. Regarding operational aspects, the primary distinction between the CL-DRM and TSTC processes lies in the inclusion of CH₄ as a feed or auxiliary gas during the reduction stage. However, in terms of the fundamental reaction principle, this change introduces a partial oxidation reaction of CH₄, subsequently lowering the reaction temperature and notably enhancing the sinter deactivation resistance of the oxygen carrier. The reaction process of CL-DRM also consists of first a reduction step:



followed by an oxidation step:



Despite the superior technical feasibility compared to TSTC, a notable drawback of the CL-DRM process lies in the utilization of CH₄, which is basically derived from fossil fuels at the current stage. Hence, the hydrogen product generated via this approach should be categorized as “blue hydrogen,” which is evidently less environmentally favorable than the “green hydrogen” produced by TSTC [8,18]. However, considering the current dominance of fossil fuels in the energy mix, the transition from traditional fossil fuels to renewable energy sources will inevitably necessitate an intermediary process or alternative. In consideration of this perspective, CL-DRM appears to hold greater promise as an intermediate solution for large-scale industrial applications [20]. Furthermore, the solar-driven CL-DRM process would gain greater research and application value once industrially recovered CH₄ is employed as the feedstock [22]. As a result, the CL-DRM reaction system is selected as the focal point of this study, with a primary goal of elucidating the challenges associated with its transition to industrial-scale implementation.

At the current stage, the principal impediment to the industrialization of CL-DRM resides in the deficiency in energy conversion. The underlying causes, from certain perspectives, predominantly manifest in the reaction kinetic, oxygen carrier, reactor design, and system-level energy management [23–25]. In comparison to related studies, this work emphasizes finding solutions to the following three issues.

(i) The limited comprehension of reaction kinetics. Present numerical modeling of the CL-DRM reaction process predominantly relies on a

combination of thermodynamics and reaction equilibrium, while giving less attention to detailed reaction kinetics, particularly the comprehensive kinetic mechanism that encompasses both gas-phase reaction and surface reaction processes. Many researchers have thermodynamically investigated the performance of the CL-DRM process using different oxygen carriers like TiO_2 [26], GeO_2 [27], or SnO_2 [28], demonstrating that the solar-to-fuel efficiency could potentially reach up to 40%. However, it is evident that current practical conversion efficiencies are significantly below this theoretical level. Thus, it is important to note that thermodynamic simulations may not accurately represent actual conversion efficiencies, whereas numerical models that incorporate detailed reaction kinetics are more valuable in elucidating the intricacies of the reaction processes. On the other hand, the CL-DRM reaction process involves complex multi-molecular gas-phase reactions and redox surface reactions of oxygen carriers, and both are essential for accurate kinetic modeling. Warren and Scheffe [29] established a surface-mediated mechanism of methane dissociation via ceria oxygen removal based on thermogravimetric experiments. The predictions of this model closely match the experimentally measured rates, indicating that the availability of surface oxygen is a crucial factor in sustaining the reaction. In conjunction with the bulk-to-surface transport equilibrium, Zhao et al. [30] developed a kinetic model for chemical looping redox reactions. The study indicates that the reduction reaction is the rate-limiting step, which determines the total amount of hydrogen produced in the subsequent oxidation step. Although several studies have been reported to determine certain surface reaction kinetic parameters through experimental methods such as thermogravimetric analysis, including all the kinetic models employed in this study, comprehensive and fundamental numerical models that incorporate the kinetics of CL-DRM gas-phase and surface reactions are still lacking in abundance.

(ii) The absence of high-performance oxygen carriers. As one of the most concerned oxygen carriers for TSTC, cerium-based oxygen carriers are likewise favored in the research on CL-DRM owing to its resistance to carbon deposition and rapid oxygen transport characteristics, primarily including non-stoichiometric cerium oxide [17] and doped cerium oxide [31]. Among those, non-stoichiometric cerium oxide ($\text{CeO}_2\text{-CeO}_{2-\delta}$) demonstrates exceptional conversion rates and high energy efficiency within the context of the CL-DRM process, and has been applied in outdoor experimental tests in conjunction with concentrating solar tower technology [32]. Nonetheless, the utilization of cerium-based oxygen carriers in CL-DRM comes with a non-negligible drawback, namely, the limited reactivity of Ce with CH_4 . As such, cerium-based oxygen carriers often require doping with additional metal elements such as vanadium (V) to enhance their reactivity [33]. On the other hand, iron-based materials that contain Ni and Fe elements have also come to be of interest [34]. As one of the extensively utilized traditional materials in high-temperature thermochemical investigations [35], iron-based oxygen carriers possess high reactivity in initial reactions, due to their robust oxygen-carrying capabilities, but face limitations attributed to catalyst deactivation caused by the oxidative densification and sintering at high temperatures. Taking into account the pronounced reactivity of the Ni element with CH_4 , the incorporation of Ni through doping typically results in a further reduction of the reaction temperature, which in turn contributes to alleviating the deactivation of iron-based oxygen carriers caused by high temperatures to a certain extent [22]. In particular, recent studies have demonstrated that the synergistic activity of iron–nickel alloys enables high CO_2 conversion and remarkable CO production [36,37]. For example, it has been reported that embedding a peroxide substrate within an iron–nickel alloy can significantly enhance the conversion of CO_2 to CO, since the alloy/substrate interface provides the primary active sites for CO_2 splitting [38]. Additionally, the incorporation of Ni has been shown to significantly enhance CO_2 conversion rates and syngas production, particularly in two-step decomposition reactions involving methane [36]. This implies that there is considerable potential for the

advancement of nickel-doped iron-based oxygen carriers in the context of CL-DRM reactions.

(iii) The inadequacy of systematic experimental demonstrations. The preparation of oxygen carriers constitutes merely the initial step towards the practical implementation of CL-DRM processes. Despite the multitude of studies focusing on the development and characterization of high-performance oxygen carriers [19,20], it is worth noting that the prepared oxygen carrier materials are typically in powder form and may not be directly applicable to experimental demonstrations of CL-DRM systems. Consequently, the application process necessitates not only the advancement of the oxygen carriers but also the development of the reaction design and the integration of the experimental system. In other words, the performance evaluation of a CL-DRM system utilizing a specific oxygen carrier is contingent on multiple factors, including reactor design, operating conditions, and the integration scheme of the system [14,39]. At present, multiple studies focusing on the systematic experimental demonstration of CL-DRM have been reported, unquestionably contributing to the progress of this technology. Examples include particle fixed-bed reaction systems [40], negative pressure reaction systems [41], volumetric reactor systems filled with foam materials [42], and integrated reactor systems combined with concentrating solar tower technology [32], among others [31,43,44]. Nonetheless, differences in oxygen carrier types, reactor designs, and experimental protocols appear to limit the comprehensiveness of existing studies in fully illustrating the developmental potential of CL-DRM processes. Consequently, further research and demonstration efforts are warranted in this domain.

Initiating from the challenges outlined above, this study conducts both numerical and experimental investigations on the solar-driven iron-based CL-DRM process. Different from mere thermodynamic predictions or the analysis of single gas-phase reaction mechanisms, a comprehensive reaction kinetic model that integrates gas-phase reactions with surface reactions is developed to shed light on the paths and patterns of material transformation. To validate the reaction performance of Ni–Fe bi-active metallic materials in the CL-DRM process, oxygen carriers are prepared by incorporating 50wt% NiO into CoFe_2O_4 nanoparticles, and are subsequently integrated with SiC ceramic foams to fabricate foam-structured materials. Guided by numerical predictions, the feasibility and noteworthy advantages of the CL-DRM process employing the prepared materials are demonstrated through a self-designed integrated thermochemical experimental platform. These research outcomes are anticipated to expedite the transition from research to industrial production for the iron-based CL-DRM reaction system.

2. Kinetic model

As one of the most representative iron-based oxygen carriers, Fe_2O_3 (Fe_3O_4) holds much significance for fundamental research [10,45,46]. In the redox process, Fe monomers and $\text{Fe}^{2+/3+}$ ions typically give rise to four common iron-based substances, denoted in the order of reduction as $\text{Fe}_2\text{O}_3 \rightarrow \text{Fe}_3\text{O}_4 \rightarrow \text{FeO} \rightarrow \text{Fe}$. These substances form the basic mechanism of the CL-DRM process when utilizing a similar type of iron-based oxygen carriers, such as NiFe_2O_4 or CoFe_2O_4 . Accordingly, a kinetic model framework describing the reaction behavior of the $\text{Fe}_3\text{O}_4/\text{FeO}$ cycle pair is established to help elucidate the basic reaction principles and pathways regarding the iron-based thermochemical process. Specifically, the kinetic model comprises two parts: the gas-phase reaction mechanism and the surface reaction mechanism. The former is based on the well-developed methane combustion mechanism GRI-Mech 3.0 [47], which includes 53 species and 325 elementary reactions, requiring mechanism reduction tailored for the CL-DRM process; the latter integrates the reaction processes of all valence state compounds of ferrite with gas components, such as CH_4 , H_2 , or O_2 , to construct the surface reaction mechanism. As a result, a comprehensive kinetic model integrating gas-phase reactions

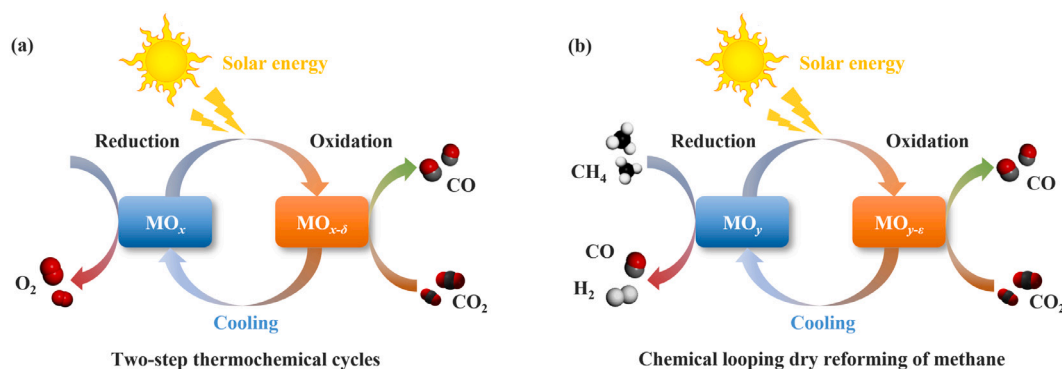


Fig. 1. Reaction principles of TSTC and CL-DRM processes [11,18].

and ferrite surface reactions for the CL-DRM process can be established. The related steady-state simulation results can provide important references for determining experimental operating parameters and analyzing experimental phenomena.

2.1. Reaction principle

To facilitate understanding and comparison, the reaction principles of the TSTC and CL-DRM processes, which are both based on the two-step oxidation–reduction procedure of metal oxides, are illustrated in Fig. 1. In the reduction step, driven by the thermal energy converted from high-flux solar energy, the metal oxide MO_x (MO_y) begins the cracking (deoxygenation) reaction upon reaching the required activation energy, while the valence state of the metal element decreases and a reduced metal oxide $MO_{x-\delta}$ ($MO_{y-\epsilon}$) is produced. In the CL-DRM process, the syngas generated during this step can serve as a direct fuel source or as a precursor for the production of various chemical products. Then, in the oxidation stage, the reaction temperature needs to be lowered together with the CO_2 (or H_2O) feed gas to facilitate the exothermic reaction in which $MO_{x-\delta}$ ($MO_{y-\epsilon}$) can be re-oxidized and regenerated to the initial state. In practical applications, the CO product derived from this step is better suited for reprocessing into various products through Fischer–Tropsch synthesis or for participation in the water–gas shift reaction to facilitate CO_2 separation and recycling.

2.2. Reaction kinetics

Despite the ostensible simplicity of the reaction principle, the CL-DRM process involves gas-phase species, site-specific (surface) species, as well as diffusive exchange between gas and solid phases at the interface, which in turn motivates the development of a chemical mechanism that couples gas-phase reactions with surface reactions. Overall, the production rate ω_k of the k th species can be expressed as a function of the stoichiometric coefficients v_{ki} and the rate-of-progress variables q_i for all reactions involving the k th species [48], mathematically,

$$\omega_k = \sum_{i=1}^I (v''_{ki} - v'_{ki}) q_i \quad (k = 1, \dots, K), \quad (3)$$

where v'_{ki} and v''_{ki} denote the forward and reverse stoichiometric coefficients, and the rate-of-progress variables q_i for the i th reaction can be determined by the difference of the forward and reverse rates as [48]:

$$q_i = k_{fi} \prod_{k=1}^K [X_k]^{v'_{ki}} - k_{ri} \prod_{k=1}^K [X_k]^{v''_{ki}}, \quad (4)$$

where X_k represents the molar concentration of the k th species, while k_{fi} and k_{ri} denote the forward and reverse rate constants of the i th reaction. It is important to note that the use of the above equation requires a fundamental assumption: the reaction order can be directly

determined by the stoichiometric coefficients. For example, in the elementary reaction $2A + B \rightarrow \text{products}$, the stoichiometric coefficient of 2 for species A directly determines that the rate-of-progress of this reaction is second-order with respect to the concentration of species A. However, for global reactions, the above assumption is typically not applicable because experimental measurements often indicate that the reaction rate may follow an arbitrary power relationship with the concentration of a species that differs from its stoichiometric coefficient. In such cases, it is necessary to use the experimentally measured reaction orders n_i instead of the stoichiometric coefficients to ensure the applicability of Eq. (4) [48].

The forward rate constants k_{fi} is typically assumed to follow the Arrhenius temperature dependence [48,49]:

$$k_{fi} = A_i T^{\beta_i} \exp\left(-\frac{E_{a,i}}{RT}\right), \quad (5)$$

where A_i is the pre-exponential factor of the i th reaction, which takes units composed of mol, cm, and s, depending on the reaction order, for instance, s^{-1} for the first order, $cm^3 mol^{-1} s^{-1}$ for the second order; β_i is the temperature exponent; $E_{a,i}$ is the activation energy, measured in $cal mol^{-1}$, and $R = 8.314 kJ mol^{-1} K^{-1}$ is the ideal gas constant.

On the other hand, the reverse rate constants k_{ri} are related to the forward rate constants through the equilibrium constants by [48]:

$$k_{ri} = \frac{k_{fi}}{K_{ci}}, \quad (6)$$

where K_{ci} is an equilibrium constant related to the reaction temperature, pressure, and thermodynamic properties. The specific calculation method can be referenced in [48].

The reaction mechanism for the gas-phase components of CL-DRM is derived from the GRI-Mech 3.0 database [47], which is one of the most widely used and comprehensive databases for simulating the combustion reactions of natural gas. However, GRI-Mech 3.0 primarily targets the simulation of natural gas combustion in devices such as internal combustion engines or boilers. Therefore, its 53 reaction species and 325 elementary reactions must undergo mechanism reduction to be applicable for CL-DRM simulations to eliminate redundant species and enhance computational efficiency. The mathematical principles of mechanism reduction are introduced in Section 2.3. On the other hand, the surface reactions are established on the basis of all the valence transition processes of the Fe_3O_4/FeO reaction pair, and the kinetic parameters of 26 surface reactions are compiled from relevant literature, as listed in Table 1. In addition, all thermal property parameters of the involved substances are supplied by GRI-Mech 3.0 and Burcat's Thermodynamic Data [50]. Finally, the gas-phase and surface reaction mechanism files in .inp format, along with the thermal properties file in .dat format, are loaded into the Ansys Chemkin 17.0 software to develop the coupled reaction mechanism. One thing to note is that although the methane cracking reaction significantly impacts the thermochemical reaction equilibrium, the developed mechanism does not

Table 1
Surface reaction kinetics of Fe₃O₄/FeO pair.

Reaction equation	A_i^a	β_i	$E_{a,i}$ (cal mol ⁻¹)	n_i	Reference
3Fe ₂ O ₃ → 2Fe ₃ O ₄ + 0.5O ₂	2.77 × 10 ¹⁴	0	116 344	1.264	Bush and Loutzenhiser [51]
3Fe ₂ O ₃ + CO → 2Fe ₃ O ₄ + CO ₂	6.20 × 10 ²	0	4778	1	Abad et al. [52]
3Fe ₂ O ₃ + H ₂ → 2Fe ₃ O ₄ + H ₂ O	2.30 × 10 ³	0	5734	0.8	Abad et al. [52]
4Fe ₂ O ₃ + CH ₄ → 8FeO + CO ₂ + 2H ₂ O	1.15 × 10 ¹⁵	0	59 964	0.56	Kang et al. [53]
Fe ₂ O ₃ + 3CO → 2Fe + 3CO ₂	1.08 × 10 ⁵	0	8839	1	Kang et al. [53]
Fe ₂ O ₃ + 3H ₂ → 2Fe + 3H ₂ O	2.24 × 10 ⁶	0	14 095	1.16	Kang et al. [53]
Fe ₃ O ₄ → 3FeO + 0.5O ₂	6.43 × 10 ¹⁵	0	176 429	3.242	Xu and Wiesner [54]
Fe ₃ O ₄ + H ₂ → 3FeO + H ₂ O	2.20 × 10 ⁸	0	30 866	–	Buelens et al. [55]
Fe ₃ O ₄ + CO → 3FeO + CO ₂	5.60 × 10 ⁻⁴	0	55 903	–	Zhu et al. [56]
Fe ₃ O ₄ + 4H ₂ → 3Fe + 4H ₂ O	3.17 × 10 ⁻⁵	0	2867	1	Jeong et al. [57]
4Fe ₃ O ₄ + O ₂ → 6Fe ₂ O ₃	3.10 × 10 ⁻²	0	3345	1	Abad et al. [52]
4FeO + CH ₄ → 4Fe + CO ₂ + 2H ₂ O	6.56 × 10 ¹³	0	54 947	0.91	Kang et al. [53]
FeO + O → Fe + O ₂	4.68 × 10 ⁻¹⁰	-0.37	729	2	NIST [58]
FeO + CO → Fe + CO ₂	7.66 × 10 ⁻¹³	0.57	972	2	NIST [58]
FeO + H ₂ → Fe + H ₂ O	1.50 × 10 ⁷	0	28 716	–	Buelens et al. [55]
3FeO + 0.5O ₂ → Fe ₃ O ₄	8.64 × 10 ⁴	0	1672	0.59	Kang et al. [53]
3FeO + H ₂ O → Fe ₃ O ₄ + H ₂	4.6 × 10 ³	0	24 392	2.872	Xu and Wiesner [54]
3FeO + CO ₂ → Fe ₃ O ₄ + CO	7.41 × 10 ⁻⁵	0	16 484	0.794	Loutzenhiser et al. [59]
Fe + O ₂ → FeO + O	1.60 × 10 ⁻⁹	-0.02	22 294	2	NIST [58]
Fe + CO ₂ → FeO + CO	2.32 × 10 ⁻¹⁰	0	28 907	2	NIST [58]
3Fe + 4H ₂ O → Fe ₃ O ₄ + 4H ₂	1.12 × 10 ⁵	0	6450	0.75	Kang et al. [53]
3Fe + 4CO ₂ → Fe ₃ O ₄ + 4CO	1.10 × 10 ⁹	0	25 897	–	Buelens et al. [55]
Fe + O ₂ → FeO ₂	2.05 × 10 ⁻²⁸	-2.6	6295	3	NIST [58]
FeO + O ₂ → FeO ₂ + O	1.02 × 10 ⁻¹¹	0.4	16 288	2	NIST [58]
FeO + CO ₂ → FeO ₂ + CO	6.48 × 10 ⁻⁹	0	45 630	2	NIST [58]
FeO ₂ → Fe + O ₂	8.42 × 10 ⁻³	-4.0	89 588	2	NIST [58]

^a A_i —pre-exponential factor, whose basic unit consists of mol, cm, s, and depends on the reaction order n_i , for instance, s⁻¹ for the first order, cm³ mol⁻¹ s⁻¹ for the second order.

incorporate relevant kinetic processes. The reason lies in the complexity of the methane cracking process, which involves intricate interactions between gas-phase carbon monomers and carbon deposition on surface sites, while there is a dearth of kinetic parameters capable of effectively describing this process. In comparison, the incorporation of inaccurate kinetic models has the potential to adversely impact the overall accuracy of the model.

2.3. Mechanism reduction

Given that the GRI-Mech 3.0 reaction mechanism includes certain species and elementary reactions that are irrelevant or less relevant to the target product, it is required to conduct a mechanism reduction to identify the core mechanism and reduce computational effort. The mechanism reduction process is principally performed with the DRGEP (directed relation graph with error propagation) algorithm and sensitivity analysis [60]. Secondary species and reaction processes that exert negligible influence on the reaction system will be eliminated from the master reaction mechanism through calculations of the coupling relationships between species, as well as the contribution of each reaction process to the major species. Aiming at identifying the direct coupling between two species and eliminating minor species, the DRGEP algorithm eliminates minor species by employing an immediate error r_{AB} , without any pre-study of the reaction system. In this process, the direct coupling relationship between species A and another species B is defined as the immediate error to the production rate of species A , introduced by the removal of another species B from the mechanism, namely [61]:

$$r_{AB} = \frac{\sum_{i=1}^I |v_{A,i} \omega_i \delta_{B,i}|}{\sum_{i=1}^I |v_{A,i} \omega_i|}, \quad \delta_{B,i} = \begin{cases} 1, & \text{if the } i\text{th reaction contains species } B, \\ 0, & \text{otherwise,} \end{cases} \quad (7)$$

where $v_{A,i}$ is the stoichiometric coefficient of species A in the i th reaction, and ω_i is the reaction rate of the i th reaction. Subsequently, once species A is retained, the other species that are directly or indirectly

coupled to A are re-examined by an “ R -value,” which determines the choice of these species, defined as [61]:

$$R_A(B) = \max_S \{r_{ij}\}, \quad (8)$$

where S denotes the set of all reaction paths from species A to species B , and r_{ij} represents the chain product of the weights of the edges along the given path.

In chemical reactions, sensitivity analysis pertains to the examination of how changes in reaction parameters impact the overall calculation results. It essentially assesses the degree of sensitivity of the calculation results to variations in the reaction parameters. Based on the sensitivity analysis, a clearer view of which elementary reactions have a greater or lesser impact on the calculation becomes available, and thus the less influential reactions can be eliminated to achieve further reduction of the reaction mechanism. The sensitivity analysis in this study is performed via Chemikin 17.0 software [48]. Since the cycling process of oxygen carriers includes two stages of reduction and oxidation, the difference between feedstock and products would severely affect the accuracy and efficiency of mechanism reduction. Consequently, the simplification of reaction mechanisms for the two stages should be handled independently, and subsequently, their concatenation can be regarded as the skeletal reaction mechanism. Concerning the mechanism simplification for the reduction stage, the essential species, which must be retained due to their direct coupling relationships, include CH₄, H₂, and CO. Conversely, for the oxidation stage, the crucial species are CO₂ and CO. The absolute tolerance of the whole mechanism reduction process is 0 with a relative tolerance of 10%; they jointly determine the maximum normalization error of the mechanism reduction process [48]:

$$E_{\text{nmax}} = \frac{|X_m - X_s|}{(R_t \times |X_m| + A_t)}, \quad (9)$$

where X_m and X_s are the values of the target species in the master and skeletal mechanisms, respectively; R_t is the relative tolerance, and A_t is the absolute tolerance.

2.4. Simulation setup

The skeletal mechanism of gas-phase components, once validated, can be integrated with the surface reaction mechanism and subsequently applied to kinetic simulations along with thermodynamic data files. Due to the complexity of gas–solid coupling reaction mechanisms, kinetic simulations are limited to steady-state calculations. Therefore, it is needed to simulate the reduction and oxidation reactions separately to obtain the reaction rates, yields, and spatial distribution of substances under different reaction conditions. On this basis, the optimal reaction temperature, feed ratio, and other parameter settings for the reduction and oxidation stages in experimental testing can be determined separately.

In the simulation cases, the geometric dimensions of the reaction cavity and the structural parameters of the ceramic foam are set to be consistent with the experimental setup. The reaction area is characterized as a porous-filled cylindrical zone with a diameter of 60 mm and a length of 80 mm, while the porosity of the ceramic foam is set to 10 PPI (pores per inch), considering a pressure drop of 10 Pa cm^{-1} [62]. The operating conditions at the gas inlet are 1 atm pressure and 1000 mL min^{-1} flow rate, with argon gas as a protective gas. The reaction temperature and feed ratio (CH_4/Ar and CO_2/Ar) are considered as variable parameters. By analyzing their effects on reaction efficiency, the optimal reaction conditions can be determined, thereby providing guidance for experimental setups. The initial oxygen carriers on the surface sites are Fe_3O_4 , with a site density of $2 \times 10^{-9} \text{ mol cm}^{-2}$ and a specific surface area of $1 \text{ m}^2 \text{ g}^{-1}$. Additionally, the absolute tolerance of the calculation process is given as 1×10^{-12} and the relative tolerance as 1×10^{-6} . The reaction process allows for non-conservation of the number of sites.

2.5. Efficiency calculation

For both simulations and experiments, the conversion of the feed gas can be calculated according to the change in mole number:

$$X_{\text{CH}_4} = \frac{F_{\text{CH}_4}^{\text{in}} - F_{\text{CH}_4}^{\text{out}}}{F_{\text{CH}_4}^{\text{in}}}, \quad (10)$$

$$X_{\text{CO}_2} = \frac{F_{\text{CO}_2}^{\text{in}} - F_{\text{CO}_2}^{\text{out}}}{F_{\text{CO}_2}^{\text{in}}}, \quad (11)$$

where F^{in} and F^{out} are the flow rates at the inlet and outlet of the solar reactor. Taking into consideration the disparity in total flow rates at the outlet and the inlet, the flow rate of each gas is determined based on the molar ratio of Ar gas.

Further, the solar-to-thermal efficiency and the net solar-to-fuel efficiency can be attained based on the energy input:

$$\eta_{\text{thermal}} = \frac{P_{\text{elec}} \cdot \eta_{\text{elec-thermal}} - Q_{\text{conv}} - Q_{\text{rad}}}{P_{\text{elec}} \cdot \eta_{\text{elec-thermal}}}, \quad (12)$$

$$\eta_{\text{solar-to-fuel, net}} = \frac{\text{HHV}_{\text{H}_2} \cdot \int r_{\text{H}_2} \text{d}t + \text{HHV}_{\text{CO}} \cdot \int r_{\text{CO}} \text{d}t - \text{HHV}_{\text{CH}_4} \cdot \int r_{\text{CH}_4} \text{d}t}{P_{\text{elec}} \cdot \eta_{\text{elec-thermal}}}, \quad (13)$$

where $\eta_{\text{elec-thermal}}$ is the electrical-to-thermal efficiency of the solar simulator, which has been determined to be 24% based on actual measurements; $\eta_{\text{solar-to-fuel, net}}$ is defined as the net solar-to-fuel efficiency, distinguishing it from the solar-to-fuel efficiency $\eta_{\text{solar-to-fuel}}$, which does not account for the heating value of methane $\text{HHV}_{\text{CH}_4} \cdot \int r_{\text{CH}_4} \text{d}t$; HHV denotes the high-level calorific value of the fuel; r_{H_2} , r_{CO} , and r_{CH_4} represent the H_2 yield, CO yield, and CH_4 feed rate, respectively; Q_{conv} and Q_{rad} are the convection and radiation heat loss from the reactor surface and quartz window, respectively, which can be gained by:

$$Q_{\text{conv}} = h_s A_s \cdot \int (T_{\text{surf}} - T_0) \text{d}t, \quad (14)$$

$$Q_{\text{rad}} = A_w \sigma \cdot \int \epsilon_w (T_{\text{reac}}^4 - T_0^4) \text{d}t, \quad (15)$$

where T_{surf} and T_{reac} represent the reactor surface temperature and internal reaction temperature, respectively, with their values obtained through experimental measurements; h_s denotes the free convection heat transfer coefficient, which is assigned the maximum value of $10 \text{ W m}^{-2} \text{ K}^{-1}$ for natural convection in air, considering the potential impact of the air cooling system in the solar simulator [63]; ϵ_w is the external emissivity of quartz window, which is determined by a polynomial of the reaction temperature [64]; σ is the Stefan–Boltzmann constant, $\sigma = 5.67 \times 10^{-8} \text{ W m}^{-2} \text{ K}^{-4}$; A_s and A_w are the heat transfer area of the reactor surface and quartz window, with the values of 331.2 cm^2 and 63.6 cm^2 , respectively, and T_0 is the environmental temperature of 298.15 K .

3. Experimental setup

All experiments in this study are conducted on a self-designed lab-scale solar thermochemical testing platform. The platform includes a solar simulator, a cavity-type thermochemical reactor, monitoring equipment, analytical instruments, gas pipelines, water-cooling circuits, and gas cylinders, enabling high-temperature thermochemical experiments up to 1600°C . In correspondence with the numerical simulations, iron-based materials are adopted as experimental oxygen carriers, whereas the distinction lies in the selective use of spinel-structured ferrite (CoFe_2O_4) and metal oxide (NiO) to enhance the reactivity and stability in practical experiments. Through physical doping, coating, and high-temperature sintering processes, the oxygen carriers are combined with SiC ceramic foam substrate to form integrated porous materials that can be directly loaded into the reaction chamber. Additionally, the operational parameters for the experimental procedure are determined by considering the simulation results, such as the optimal steady-state reduction temperatures, and further refined in conjunction with the experimental analysis results. Detailed information regarding the experimental platform, material preparation, and experimental procedures is provided in the following subsections.

3.1. Experimental platform

Figure 2 gives an overview of the lab-scale high-temperature solar thermochemical testing platform, including both the system constituents and operation principle. A solar simulator consisting of three identical xenon lamps, each with a rated power of 6 kW, is used as an alternative power source to produce stable and high-flux solar energy. The total output power of the simulator can be continuously adjusted in the range of 1.5 to 18 kW through the power controllers of each xenon lamp. The concentrated rays, after passing through the quartz window installed at the front of the solar reactor, are absorbed by the SiC ceramic foam within the reaction chamber, and thus create a high-temperature environment conducive to endothermic reactions [65]. The selected oxygen carrier nanoparticles are coated on the surface of the SiC substrate, converting thermal energy into chemical energy through a series of substance diffusion and chemical reactions at the gas–solid interface [64]. High-purity (99.999%) feed gases, CH_4 and CO_2 , with Ar as the carrier gas, are delivered into the solar reactor under the control of mass flow meters (SIERRA Smart-Trak 2, control accuracy of $\pm 1.0\%$), and the product composition is analyzed using a custom-made gas chromatograph (SCION GC-456C, relative standard error less than 1.5%). The reaction temperature and insulation temperature are measured using type S and K armored thermocouples (with a measurement error of $\pm 1.5^\circ\text{C}$), respectively. It should be noted that the S-type thermocouple probe is placed at the midpoint along the axial direction of the reaction chamber, making direct contact with the circumferential surface of the porous ceramic foam, but not embedded within the foam material so as to minimize measurement errors caused

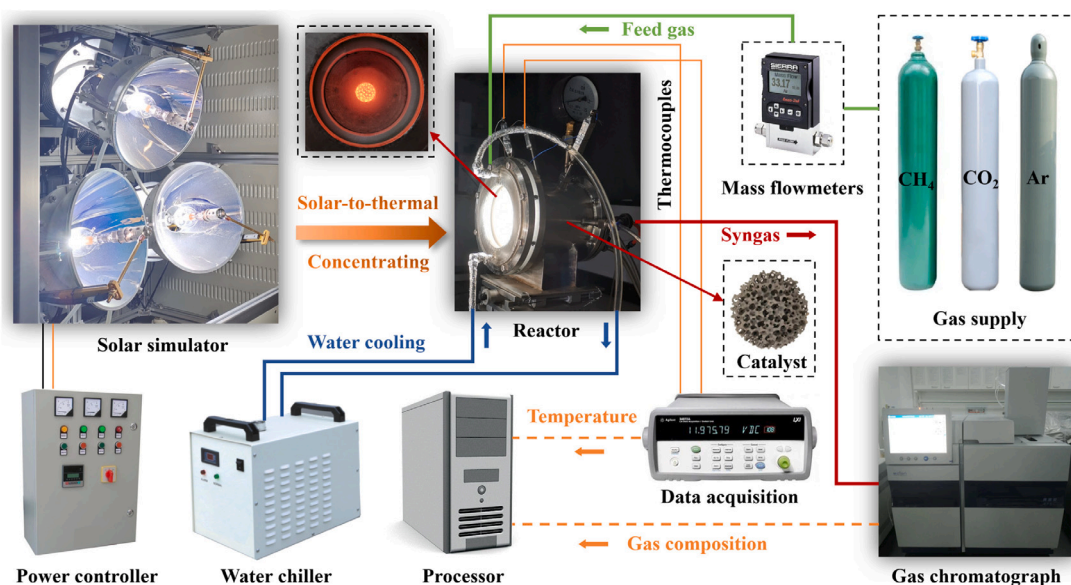


Fig. 2. Experimental setup for high-temperature solar thermochemical cycles.

by direct light exposure. Subsequently, the electrical signal from the thermocouples is read at 10-s intervals by the data acquisition unit (AGILENT 34972 A, with an accuracy of $\pm 0.004\%$) and converted into a digital temperature signal displayed at the control terminal. Based on this, precise control of high-temperature thermochemical reaction conditions, as well as real-time monitoring of reaction states and products, can be achieved.

The solar reactor, serving as a fundamental component within the solar thermochemical system, plays a crucial role in shaping the energy conversion efficiency of the overall reaction process [32]. In this study, the solar reactor is designed with a direct-radiating cavity structure, featuring a cylindrical cavity that measures 80 mm in length and 60 mm in diameter. This design allows concentrating solar energy to directly irradiate the surface of the filled reaction materials, offering the advantage of high initial conversion efficiency of solar energy to thermal energy. However, it typically comes with significant high-temperature reradiation losses through the optical window. Therefore, optimizing structures such as apertures is necessary to enhance the final solar-to-thermal efficiency [66]. Depending on the type of material, the entire reactor can be roughly divided into two layers. The outer layer is made of stainless steel, serving as a high-strength supporting framework, as well as various measurement components such as thermocouples and pressure gauges. The inner layer consists of at least 40-mm-thick Al_2O_3 insulating ceramic, whose geometric structure determines the dimensions of the front radiation-receiving surface, aperture, and the reaction cavity. Specifically, the radiation-receiving surface is designed in a funnel shape, and its integration with the reaction chamber creates a through-hole with a diameter of approximately 40 mm, referred to as the aperture [62]. The primary purpose is to allow the passage of high-density solar rays while minimizing the outward transmission of radiation energy from the interior of the high-temperature reaction chamber. Additionally, water-cooled channels are reserved in the flanges at the front and rear ends of the solar reactor, serving to alleviate the problem of thermal stress concentration and simultaneously cool the outlet gas.

3.2. Material preparation

Based on a couple of previously reported theoretical and experimental investigations concerning the selection and evaluation of iron-based

oxygen carriers [67,68], it has been determined that CoFe_2O_4 displays the highest levels of reactivity and cycling stability among six ferrate salts (comprising Fe, Ni, Co, Cu, Zn, Sr) in the current reaction system. Additionally, NiO, selected from a pool of four metal oxide dopants (including ZrO_2 , CeO_2 , NiO, and Co_3O_4), is capable of augmenting the reactivity of CoFe_2O_4 by approximately 70%. Moreover, the natural reactivity of the Ni element towards CH_4 makes this doped oxygen carrier highly suitable for the CL-DRM reaction process. As such, 50wt% CoFe_2O_4 -NiO nanoparticles (abbreviated as 50%CF-Ni) are selected as the oxygen carrier and subsequently coated onto the surface of high-porosity SiC ceramic foams to prepare foam-structured materials (FSM). Specifically, equal mass fractions of commercial CoFe_2O_4 nanoparticles (particle size < 100 nm, purity $\geq 99\%$) and NiO nanoparticles (particle size < 30 nm, purity $\geq 99.5\%$) are mixed in an ethanol solution and subjected to ultrasonic treatment at room temperature for 30 min. The resulting slurry is then coated onto the surface of SiC ceramic foam and allowed to air dry. After that, the coated foam is calcined in a muffle furnace at 900°C for 6 h to produce the 50wt% CoFe_2O_4 -NiO@SiC (abbreviated as 50%CF-Ni@SiC) FSM. For this study, the total loading of the 50%CF-Ni is 8.7 ± 0.1 g, while the weight of the SiC substrate is 45.5 ± 0.1 g with a pore size of 10 PPI. The detailed preparation method, along with the microscopic characterization and analysis of the oxygen carrier before and after the reaction, can be referenced in our previous work [67].

3.3. Experimental procedure

According to the reaction principle of two-step oxidation-reduction cycling, the experimental procedure consists of alternating cycles of a higher temperature reduction process and a lower temperature oxidation process, in which the temperature control is performed by an electrical power controller of the solar simulator. Apart from the initial preheating phase at approximately 200°C for around 10 min, the entire reaction process can be divided into four steps, which alternate cyclically:

(i) Heating step. Under an argon atmosphere at a flow rate of 400 mL min^{-1} , the reaction temperature is rapidly increased by maintaining a total electrical power of 4.5 kW across three xenon lamps. The target temperature for this step is primarily determined by the optimal reduction temperature obtained from simulation analysis. Through real-time online temperature monitoring, once the target temperature is reached, the next step is executed.

(ii) Reduction step. Maintaining the xenon lamp power and the total gas flow rate constant, the feed gas is delivered to the solar reactor according to the CH_4/Ar ratio provided by the simulation analysis, under the control of mass flow meters. Due to the strongly endothermic nature of the reduction reaction, a significant drop in reaction temperature might be observed during this step.

(iii) Cooling step. Under a pure argon atmosphere at 400 mL min^{-1} , the power of the xenon lamps is reduced to 1.5 kW. As a result, the reaction temperature rapidly decreases due to heat loss exceeding the input energy. This process continues until a relatively steady state is reached due to the energy balance.

(iv) Oxidation step. Maintaining the xenon lamp power and total flow rate constant, the oxidation reaction is conducted according to the optimal CO_2/Ar ratio provided by the simulation analysis. Since the oxidation reaction is exothermic, the reaction rate under the current conditions is relatively slow, requiring more time than the reduction step.

Note that the duration of each step is determined by the heating/cooling rates and the syngas production rate. In this study, the reduction step lasts for 15.5 min, while the oxidation step lasts for 25 min. Additionally, the total gas flow rate set in the experiment is lower than that used in the simulation. This adjustment is due to the limitations of the gas chromatography online detection interval, as a lower flow rate allows for more detailed information on yield variations to be obtained.

4. Result and discussion

This section is subdivided into three parts. In Section 4.1, the ultimate skeletal mechanism attained through mechanism reduction is presented to clarify the CL-DRM reaction process. Following this, Section 4.2 expounds upon the detailed reaction pathways and characteristics of the CL-DRM based on the developed reaction mechanism. This section unveils the underlying mechanism that enables the CL-DRM process to attain a high syngas yield at relatively low temperatures. Finally in Section 4.3, experimental tests are conducted to validate the accuracy of the numerical method based on the numerical prediction results of the reaction characteristics. This section also assesses the potential applicability of the CL-DRM process.

4.1. Outcome of mechanism reduction

Figure 3 color-codes the simplified results of the gas-phase species within the two stages of reduction and oxidation. The gray zone represents the 39 species eliminated through mechanism reduction; the light yellow zone denotes the 7 core species (including $\text{H}_2/\text{CH}_2/\text{CH}_2(\text{S})/\text{CH}_3/\text{CH}_4/\text{Ar}$) that were reserved only in the reduction stage; the blue zone indicates the 2 core species (including HCO/O) that were kept only in the oxidation phase; and the green zone refers to the 4 core species (including $\text{H}/\text{OH}/\text{CO}/\text{CO}_2$) that were commonly preserved in the two stages. Note that Ar, as an inert carrier gas used to lower the explosive limits of syngas, typically does not directly participate in chemical reactions. However, it can still influence simulation and experimental results for three reasons. First, the proportion of Ar is directly related to the volumetric fractions of various reactive gases, thereby affecting the reaction equilibrium. Second, Ar can participate in certain surface site replacement reactions, such as $\text{CH}_2(\text{S}) + \text{Ar} = \text{CH}_2 + \text{Ar}$. Third, considering the non-conservation of the total gas volume during the experimental process, Ar, as the only stable flow reference, can be used to correct the outlet flow rates of other gases. Furthermore, as an indispensable gas-phase reactant for surface reactions, the O_2 species was maintained as well. It is worth noting that while the methane cracking reaction ($\text{CH}_4 \rightarrow \text{C} + 2\text{H}_2$) typically plays an important role in thermochemical reactions, particularly those involving nickel oxides, the kinetics for the transformation of cracked gaseous C monomers into solid C monomers at the surface site remains

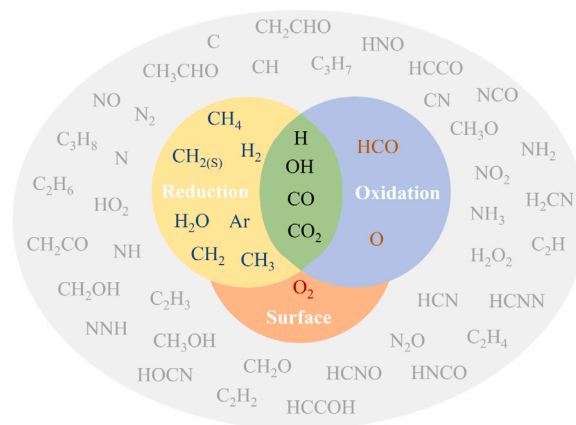


Fig. 3. Screening of the core species in the mechanism reduction process. The gray area represents the gas-phase components eliminated through mechanism reduction; the yellow area denotes components retained only in the reduction step; the blue area indicates components retained only in the oxidation step; the green area signifies components retained in both reduction and oxidation steps; and the orange area represents components that must be retained due to surface reactions. (For interpretation of the references to color in this figure legend, the reader is referred to the web version of this article.)

unclear. Consequently, unwarranted adoption of the carbon deposition reaction mechanism could diminish the overall computational accuracy of the kinetic model. For a detailed exploration of carbon deposition behavior in gas-phase reactions, we recommend referring to our prior work on this topic [69]. Ultimately, the simplified mechanism involving reduction and oxidation stages is summarized to develop a core reaction mechanism document that contains 14 gas-phase species and 5 surface species.

Table 2 compares the numbers of species and reactions for each process before and after the mechanism reduction. For the surface reactions, all reaction kinetic data have been retained since the current species and reactions are not redundant; for the gas-phase reactions, the number of species was simplified from 53 to 14, while the number of reactions was reduced from 325 to 26, with the relevant reaction kinetic parameters listed in Table 3. Owing to the decreased number of reactions, the required calculation for the mechanical simulation could be reduced by approximately 85%. Furthermore, as the ultimate core reaction mechanism is derived from the amalgamation of the simplified reduction process, oxidation process, and surface reactions, this approach guarantees the highest possible simulation accuracy for the CL-DRM process.

Prior to applying the skeletal mechanism to elucidate the pertinent reaction characteristics and pathways, it is imperative to confirm that the mechanism reduction procedure maintains simulation accuracy in its impact on the calculation results. Figure 4 illustrates the validation of the skeletal mechanism with the master mechanism at different temperatures. Note that, aside from the differences in gas-phase mechanism files, the other parameter settings in the validation cases, such as reactor geometry, reaction conditions, and site concentration, are completely identical. Due to the reduction of the original 325 gas-phase elementary reactions to only 26, the calculation results for syngas yield are inevitably affected, especially within the temperature range of 1000–1050 K. However, the overall trend remains highly consistent, showcasing substantial agreement across other temperature ranges. In the case of the oxidation process, the simplification of the mechanism has minimal impact on the calculation accuracy. Overall, the computational errors resulting from the current mechanism reduction process fall within an acceptable range. This ensures that the reduction in mechanism complexity does not compromise simulation reliability, while notably accelerating calculation speed.

Table 2
Comparison of species and reactions before and after mechanism reduction.

Item	Master mechanism		Skeletal mechanism		Retained gas species
	Species	Reaction	Species	Reaction	
Reduction stage	53	325	11	21	H/OH/H ₂ /H ₂ O/CO/CO ₂ /CH ₂ /CH ₂ (S)/CH ₃ /CH ₄ /Ar
Oxidation stage	53	325	6	6	H/OH/CO/CO ₂ /HCO/O
Surface reaction	5	26	5	26	O ₂
Summary	58	351	19	52	H/OH/H ₂ /H ₂ O/HCO/O/CO/CO ₂ /CH ₂ /CH ₂ (S)/CH ₃ /CH ₄ /Ar/O ₂

Table 3
Skeletal gas-phase reaction kinetics attained by mechanism reduction.

Reaction equation	A_i^a	β_i	$E_{a,i}$ (cal mol ⁻¹)	Reaction equation	A_i	β_i	$E_{a,i}$ (cal mol ⁻¹)
2H + M = H ₂ + M	1×10^{18}	-1	0	CH ₂ + H ₂ = H + CH ₃	5×10^5	2	7230
2H + H ₂ = 2H ₂	9×10^{16}	-0.6	0	CH ₂ + CH ₄ = 2CH ₃	2×10^6	2	8270
2H + H ₂ O = H ₂ + H ₂ O	6×10^{19}	-1.25	0	CH ₂ (S) + Ar = CH ₂ + Ar	9×10^{12}	0	600
2H + CO ₂ = H ₂ + CO ₂	5.5×10^{20}	-2	0	CH ₂ (S) + H ₂ = CH ₂ + H	7×10^{13}	0	0
H + OH + M = H ₂ O + M	2.2×10^{22}	-2	0	CH ₂ (S) + H ₂ O = CH ₂ + H ₂ O	3×10^{13}	0	0
H + CH ₂ (+M) = CH ₃ (+M)	6×10^{14}	0	0	CH ₂ (S) + CH ₂ = 2CH ₂	1.6×10^{13}	0	-570
H + CH ₃ (+M) = CH ₄ (+M)	1.39×10^{16}	-0.534	536	CH ₂ (S) + CO = CH ₂ + CO	9×10^{12}	0	0
H + CH ₄ = CH ₃ + H ₂	6.6×10^8	1.62	10 800	CH ₂ (S) + CO ₂ = CH ₂ + CO ₂	7×10^{12}	0	0
OH + H ₂ = H + H ₂ O	2.16×10^8	1.51	3430	O + H + M = OH + M	5×10^{17}	-1	0
OH + CH ₃ = CH ₂ + H ₂ O	5.6×10^7	1.6	5420	O + CO(+M) = CO ₂ (+M)	1×10^{10}	0	2390
OH + CH ₃ = CH ₂ (S) + H ₂ O	6.44×10^{17}	-1.34	1420	O + HCO = OH + CO	3×10^{13}	0	0
OH + CH ₄ = CH ₃ + H ₂ O	1×10^8	1.6	3120	O + HCO = H + CO ₂	3×10^{13}	0	0
OH + CO = H + CO ₂	4.76×10^7	1.228	70	HCO + M = H + CO + M	1.87×10^{17}	-1	17 000

^a A_i —pre-exponential factor, with composite units consisting of mol, cm, and s, depending on the reaction order n_i . For instance, s⁻¹ for the first order, cm³ mol⁻¹ s⁻¹ for the second order.

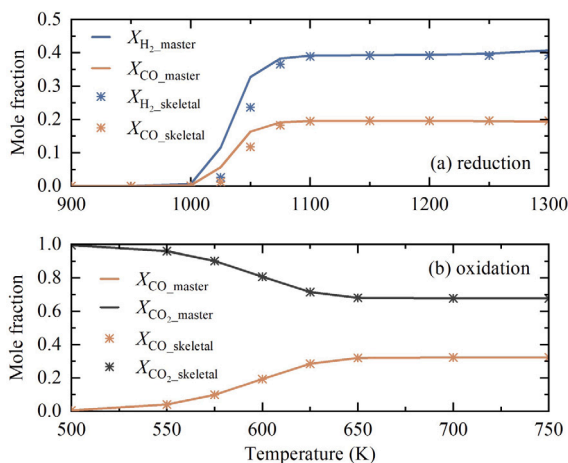


Fig. 4. Validation of the skeletal mechanism with the master mechanism under different temperatures at (a) reduction stage and (b) oxidation stage.

4.2. Reaction characteristics and reaction paths

Figure 5 depicts the impact of methane feed ratio on the reactivity of Fe₃O₄ oxygen carrier and syngas production at different reduction temperatures. Herein, the chemical reactivity of Fe₃O₄ is defined as the percentage of the site density of Fe₃O₄ that has been reduced to FeO or Fe relative to the initial site density. As such, the temperature at which the chemical reactivity value begins to increase above zero can be regarded as the activation temperature of the oxygen carrier. In these cases, the total gas flow rate is set to 1000 mL min⁻¹, with an operating pressure of 1 atm. It should be noted that, since the kinetic simulations are conducted under fixed-temperature conditions, changes in flow rate do not affect the reaction temperature but determine the residence time of the reactive gases within the reaction vessel, thus directly influencing the simulation results. As demonstrated in Fig. 5a, under the conditions in the absence of the auxiliary reducing gas, i.e., a pure Ar atmosphere, the Fe₃O₄ oxygen carrier begins to decompose

at approximately 1800 K, of which the reaction equation is Fe₃O₄ → 3FeO + 0.5O₂. After adding CH₄ auxiliary gas, the decrease in reduction temperature of the oxygen carrier is clearly evident, in that, Fe₃O₄ starts to decompose at about 1050 K, with a much higher reaction rate than that in a pure Ar atmosphere. At this point, according to the analysis of the reaction path, the main reaction occurring in the Fe₃O₄ oxygen carrier is Fe₃O₄ + H₂ → 3FeO + H₂O. In this reaction, H₂ must be derived from the decomposition of CH₄, though the relevant reaction process is relatively complicated, which is temporarily deferred but explained in the subsequent analysis of the reaction path. For now, it can be inferred that compared to the direct reduction pathway of Fe₃O₄ by CH₄, CH₄ more readily undergoes decomposition to produce H₂, which in turn reduces Fe₃O₄. This CH₄ → H₂ → Fe₃O₄ reduction pathway has been confirmed by previous studies, especially at reaction temperatures below 1273 K [70].

From the perspective of the chemical activity of Fe₃O₄, increasing the CH₄ content in the feed gas from 25% to 75% has almost no quantifiable effect on the reduction temperature and conversion rate. This phenomenon can be attributed to the prevailing operating conditions, characterized by low-level utilization of oxygen carriers and a relatively high feed gas flow rate. Under these conditions, the primary factor influencing the reduction degree of the oxygen carriers is not the methane gas content but rather the kinetic limitations at the present reaction temperature. In contrast, the auxiliary gas with an “extreme” case of 1.0% content apparently does not enable the complete reduction of the oxygen carrier below the reaction temperature of 1800 K. Nevertheless, the addition of 1.0% CH₄ can already lower the required reduction temperature quite significantly, while enhancing the reaction activity of the oxygen carriers substantially.

Although the percentage of CH₄ in feed gas seems rather inconsequential thus far, it is, in fact, of considerable importance for the final syngas yield at the outlet. Figure 5b presents the variation in the mole fraction of syngas product with different levels of CH₄ auxiliary gas at 1000 K and 1100 K reduction temperatures. Under conditions where the CH₄ content is below 30%, there is a noticeable improvement in syngas yield as the CH₄ content increases, as well as a more remarkable enhancement in H₂ yield. Whereas, once the added methane content exceeds 30%, the enhancement of syngas production is no longer significant. Moreover, the H₂/CO ratio of the syngas remains

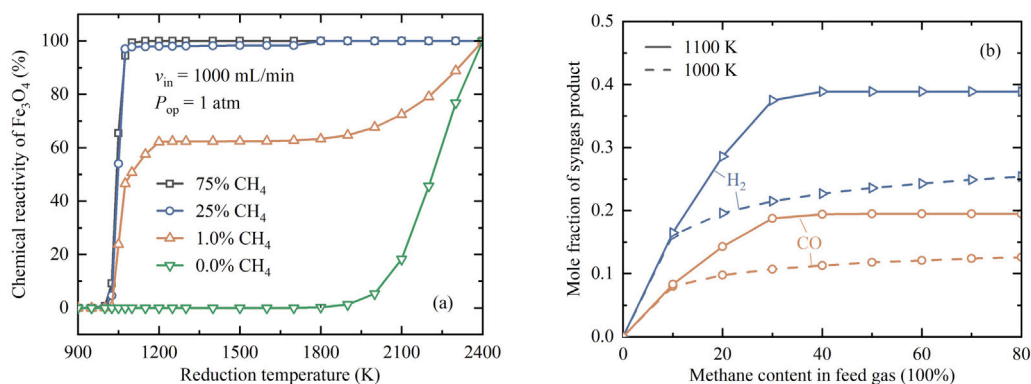


Fig. 5. Effects of methane content in feed gas on the reduction stage: (a) chemical reactivity of the oxygen carrier; (b) mole fraction of syngas.

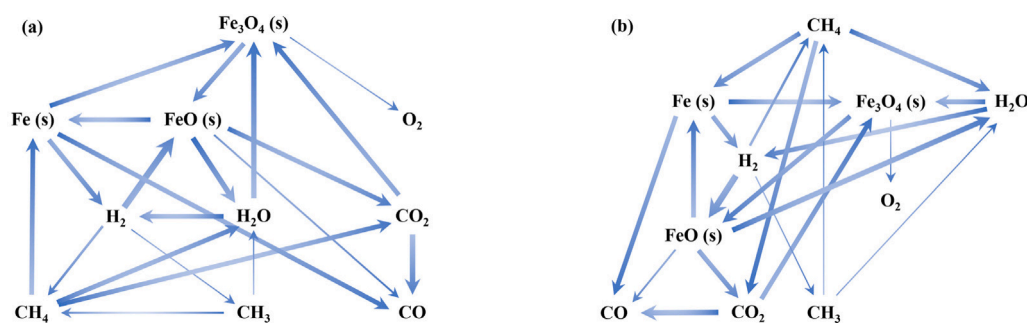


Fig. 6. Detailed reaction path of the reduction process (1100 K, 20% CH₄): (a) main reaction path of the oxygen carrier (Fe₃O₄); (b) main reaction path of the feed gas (CH₄). The arrows signify the direction of reactant conversion, and the thickness of the arrows reflects the reaction trend or reaction rate for each step.

essentially at 2:1, aligning perfectly with the theoretical product ratio of CH₄ decomposition. Also worth noting is that the syngas yields at two different temperatures are nearly identical when the CH₄ content in the feed gas is below 10%. This suggests that within the current temperature range, the reaction rate is predominantly constrained by the content of CH₄ auxiliary gas rather than the reaction kinetics. In essence, adding more than 10% CH₄ auxiliary gas proves to be an effective method for augmenting the syngas yield. However, at the current operating conditions, complete conversion of CH₄ into syngas is not achieved. Therefore, a 10% addition appears to strike a good balance in terms of attaining an optimal cost–benefit ratio.

Considering the calculation example at a reduction temperature of 1100 K and a 20% CH₄ auxiliary gas addition, Fig. 6a and b illustrate the comprehensive reaction pathways of the reduction process, commencing with the oxygen carrier (Fe₃O₄), and the feed gas (CH₄), respectively. Note that the reaction processes and the species involved are identical in both subfigures, differing only in terms of presentation. While the arrows signify the direction of reactant conversion, the thickness of the arrows reflects the reaction trend or reaction rate for each step in the reaction process.

Under the current reaction conditions, the decomposition of Fe₃O₄ oxygen carrier to FeO mainly follows two reaction paths, they are, direct cracking and hydrogenation reduction. Obviously, the decomposition process of Fe₃O₄ oxygen carrier depends primarily on the presence of a H₂ atmosphere, as the reaction rate of direct deoxygenation is extremely low at the current reaction temperature. An analysis of the entire reaction pathway underscores the significance of the FeO species as a crucial intermediate in the CL-DRM process. On one hand, FeO serves as the principal pathway for the decomposition of Fe₃O₄ oxygen carriers at the prevailing temperature. On the other hand, it can undergo further reduction into Fe monomers within the methane-enriched atmosphere, a process represented by the equation: $4\text{FeO} + \text{CH}_4 \rightarrow 4\text{Fe} + \text{CO}_2 + 2\text{H}_2\text{O}$. This equation represents another

vital reaction in the reduction process. The resulting product contains strongly reducing Fe monomers, enabling the direct reduction of H₂O and CO₂ into H₂ and CO. Additionally, it leads to the transformation of Fe back into the initial Fe₃O₄ state. The primary reactions for the regeneration of oxygen carriers are: $3\text{Fe} + 4\text{H}_2\text{O} \rightarrow \text{Fe}_3\text{O}_4 + 4\text{H}_2$, $3\text{Fe} + 4\text{CO}_2 \rightarrow \text{Fe}_3\text{O}_4 + 4\text{CO}$. Furthermore, the intermediate product FeO also possesses the capability for CO₂ reduction, although the reaction rate is relatively slow. The reaction equation for this process can be represented as $3\text{FeO} + \text{CO}_2 \rightarrow \text{Fe}_3\text{O}_4 + \text{CO}$. Following this, the reduced H₂ participates in the initial decomposition reaction of Fe₃O₄ oxygen carrier, leading to the formation of FeO surface species once more. The processes mentioned above are the primary factors and reaction pathways responsible for the reduction of Fe₃O₄ oxygen carriers and the production of H₂ and CO products. It follows that the sequence of the oxygen carrier reduction process under a CH₄-assisted atmosphere can be summarized as Fe₃O₄ → FeO → Fe. From the analysis of the final product, the Fe₃O₄ oxygen carrier is basically consumed once the entire reaction system reaches an equilibrium state. On the other hand, the reaction path illustrated in Fig. 6b, with CH₄ as the initial species, relies on the same reaction principle, while the only difference lies in the starting point being viewed from a different perspective. Actually, there are also many interconversions between gas-phase species in the process, such as H₂ → CH₃, CH₃ → CH₄, CH₃ → H₂O, etc. Compared to surface reactions, these gas-phase reactions have lower rates and minimal effects on the overall reaction pathways, and as a result, they are not described in detail.

In the current cycle process, the active component on the surface sites during the oxidation stage is primarily composed of Fe monomers. These Fe monomers possess strong reducing properties, enabling them to effectively convert CO₂ into CO and thus regenerate the oxidized oxygen carriers. The impact of CO₂ content on the regeneration rate of Fe₃O₄ (Fe → Fe₃O₄, which can also be interpreted as the fraction of surface sites), as well as on the CO yield, is illustrated in Fig. 7a

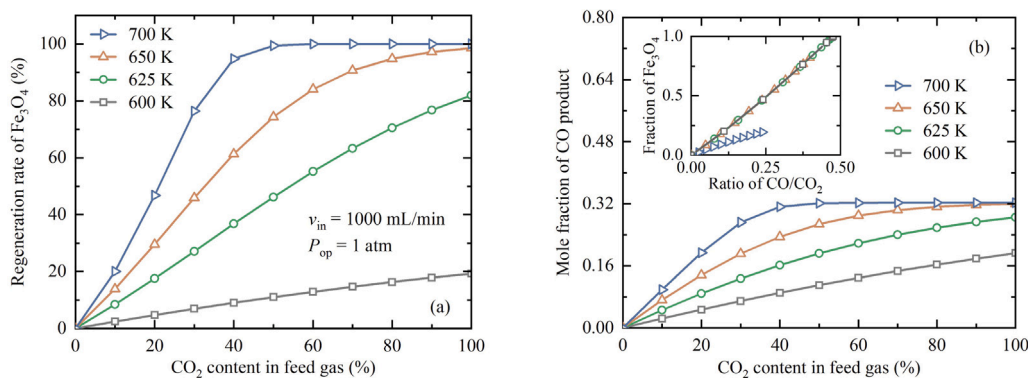


Fig. 7. Effects of CO₂ content in feed gas on the oxidation stage: (a) regeneration rate of the oxygen carrier; (b) mole fraction of CO product.

and Fig. 7b, respectively. It is apparent that either raising the reaction temperature or increasing the CO₂ content is capable of consistently improving CO yield and oxygen carrier conversion within a certain range. However, limited by the reaction kinetics and usage of oxygen carriers, further adjustments to operating conditions no longer have a significant impact on feedstock conversion and CO production when the reaction temperature or CO₂ content is increased to a certain value. For instance, once the CO₂ content reaches 100%, an oxidation temperature of 650 K is sufficient to completely convert the Fe monomers back into the original Fe₃O₄. In this case, the CO mole fraction in the product remains around 0.32 despite continuously raising the oxidation temperature. Likewise, a CO₂ content of 50% at 700 K yields the highest CO production under the current reaction conditions. Moreover, the subplot in Fig. 7b illustrates the relationship between the CO/CO₂ ratio and the site fraction of Fe₃O₄ at different oxidation temperatures. Clearly, at temperatures exceeding 625 K, the oxidation state of the ferrite oxygen carrier under reaction equilibrium is almost entirely dependent on the CO/CO₂ ratio and is independent of the reaction temperature. That is, once a sufficient oxidation temperature is reached, the regeneration rate of Fe₃O₄ can be adjusted by controlling the CO/CO₂ ratio [71,72].

Compared to the reduction process, the reaction paths of the oxygen carriers in the oxidation stage are relatively straightforward. As shown in Fig. 8a, under the action of Fe monomers, the majority of the CO₂ feed gas is reduced into CO at the initial position of the reaction zone, while another small amount of CO₂ oxidizes Fe monomers into the intermediate product FeO. This process can be expressed as $\text{Fe} + \text{CO}_2 \rightarrow \text{FeO} + \text{CO}$. Subsequently, the FeO continues to participate in the reduction process of CO₂. In contrast, the reaction path inside the reactor is somewhat more complex. As shown in Fig. 8b, the majority of Fe monomers on the surface site regenerate into Fe₃O₄, with the remaining portion transforming into FeO, consistent with the reaction steps at the initial position. The difference is that the FeO intermediate at this site is generated by three additional pathways: one involves the direct interaction of Fe monomer with H₂O to generate FeO and release H₂; the second is the partial oxidation of Fe monomer by O₂ to form FeO directly; while the third is the combination of FeO₂ with CO to generate FeO. Although the presence of intermediate FeO facilitates CO₂ conversion, the reaction rates of the above three pathways remain at low levels, and thus their ultimate contribution to CO production is not significant.

4.3. Experimental validation and analysis

To validate the accuracy of the numerical calculations, experiments were conducted on the developed experimental platform for high-temperature solar-driven CL-DRM processes. As predicted by the numerical simulations, the optimal reaction temperature for the reduction step of the CL-DRM process is around 1150 K, whereas that for

oxidation is approximately 650 K. Following this operating condition, Fig. 9 indicates the syngas yield per unit mass of the prepared oxygen carrier under five non-isothermal cycles; the blue background region denotes the CH₄ gas atmosphere (CH₄:Ar = 1:3), and the gray region represents the CO₂ gas atmosphere (CO₂:Ar = 1:1), with the total flow rate kept constant at 400 mL min⁻¹. In the experiment, a single 1.5 kW xenon lamp was turned on first to preheat the solar reactor to about 200°C, and then three lamps (4.5 kW total) were operated to accelerate the heating to around 1173 K. At this point, the entrance of the CH₄ auxiliary gas obviously reduced the reaction temperature, which is mainly attributed to the fact that the CH₄ undergoes a highly endothermic partial oxidation reaction and takes away a large amount of heat, thus resulting in a direct decrease of the reaction temperature. The temperature curve, in combination with the subsequent increase in temperature after shutting off the methane gas, demonstrates a direct correlation between the CH₄ atmosphere and temperature changes. After that, only one 1.5 kW xenon lamp was retained to reduce the temperature until about 773 K, at which point CO₂ feed gas was introduced to initiate the oxidation reaction process. The entire oxidation step lasted about half an hour, after which the CO₂ was turned off and the three lamps were turned on again for the next cycle until completing the five thermochemical cycles.

As indicated by the syngas yield per unit mass of the oxygen carrier, the highest H₂ yield in the reduction stage is 23.5 mL min⁻¹ g⁻¹, and the highest CO yield is 11.6 mL min⁻¹ g⁻¹. After five cycles, the peak H₂ yield decreased to 21.6 mL min⁻¹ g⁻¹, which is 8.1% lower compared to the first cycle. On the other hand, the peak CO yield in the oxidation stage eventually decreased as well, but with a different trend. Interestingly, except for the first cycle, the peak CO yield within a single cycle typically appears in the heating stage after turning off the CO₂ gas. Intuitively, it seems that the critical factor leading to the sudden increase in CO yield at this stage is the rise in reaction temperature, which means that increasing the oxidation temperature might be conducive to improving CO production, as observed in our previous study on the TSTC reaction system [67]. Furthermore, Fig. 10 illustrates the conversion rates of CH₄ and CO₂ feed gases during the five non-isothermal cycles. The green and gray regions indicate the control amounts of CH₄ and CO₂ at the gas input, respectively. The conversion of CH₄ auxiliary gas during the reduction stage was at a high level, with its peak remaining at around 90%. In contrast, the peak CO₂ conversion reached 46% in the first cycle, while those in the other cycles were approximately 30%. The above data revealed that much potential is still available for further optimization of the operating parameters under the current reaction system.

Based on the integral calculation of the measured gas concentrations, the total syngas yields of the reduction and oxidation stages were obtained separately, as depicted in Fig. 11. In general, the output of H₂ in the reduction stage was relatively stable, and the total output within a single cycle was maintained above 4 L. Meanwhile, a small amount

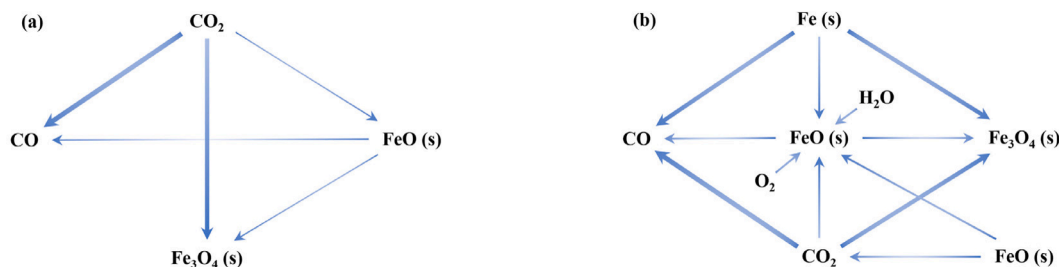


Fig. 8. Detailed reaction path of the oxidation stage (650 K, 40% CO₂): (a) main reaction path of the feed gas (CO₂) at the initial position of the reactor; (b) main reaction path of the reduced oxygen carrier (Fe) at $x = 20$ mm.

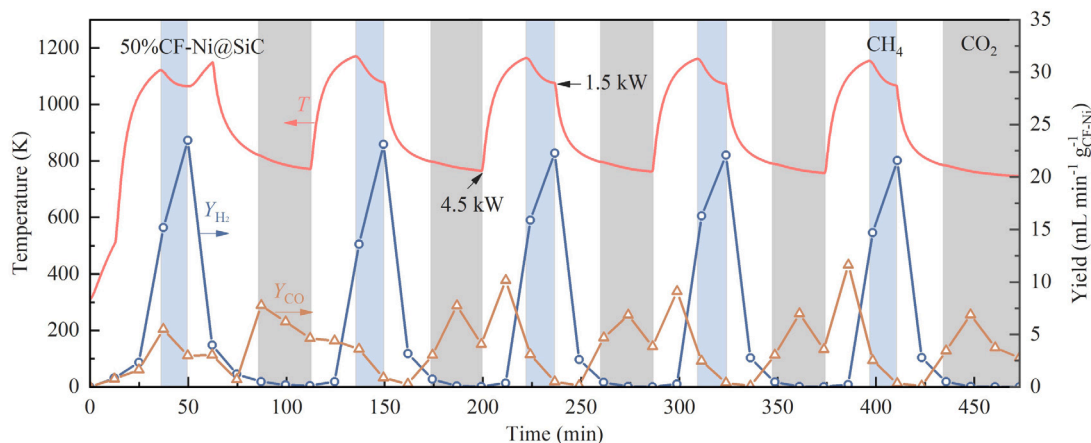


Fig. 9. Variation of the reaction temperature (refer to the left axis) and syngas yield (refer to the right axis) under five cycles [73]. The abbreviation 50%CF-Ni@SiC refers to the foam-structured material created by applying a coating of an oxygen carrier, resulting from the doping of an equal mass of CoFe₂O₄ with NiO, onto the surface of SiC foam ceramics. (For interpretation of the references to color in this figure legend, the reader is referred to the web version of this article.)

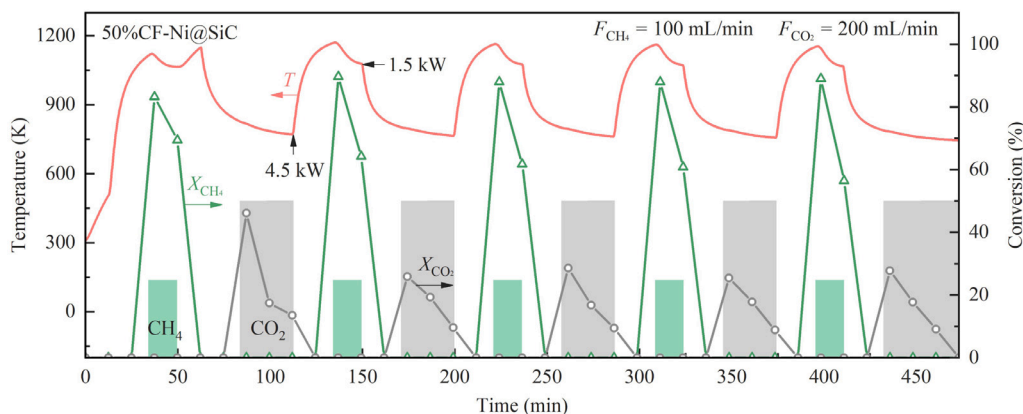


Fig. 10. Conversion rate of the feed gases (refer to the right axis) under five cycles of the CL-DRM process.

of CO is produced in the reduction process, and the total amount shows a noticeable decline after five cycles. Theoretically, the complete decomposition of CH₄ in the reduction stage is supposed to produce syngas with a H₂/CO ratio of 2. But after five cycles, the ratio of H₂ to CO production exceeds 13. Combined with the conversion rate curves of CH₄ and CO₂ in Fig. 10, it is speculated that a methane cracking reaction (CH₄ → C + 2H₂) might have occurred in this process, as a CO₂ conversion rate of zero indicates that the reaction pathway does not involve the partial oxidation of methane (CH₄ + O → CO + 2H₂) followed by the reoxidation of CO to CO₂. At the same time, the carbon particles produced by methane cracking could block the active sites on the surface of the oxygen carriers and reduce the cycling stability of the material to some extent [74]. Based on our prior study [67], carbon deposition during high-temperature thermochemical reactions

involving nickel-containing oxygen carriers typically occurs through two distinct mechanisms: the direct deposition of carbon monomer and the formation of NiC_x through interaction with nickel. The former can be mitigated by promoting the disproportionation reaction of CO (also known as the Boudouard reaction, C + CO₂ → CO), thereby facilitating the restoration of active sites on the oxygen carriers. However, the latter lacks a clearly defined elimination pathway for the time being, necessitating further investigations to elucidate the underlying reaction mechanism. Hence, within the present operational conditions, it is reasonable to hypothesize that the equilibrium between these two processes collectively governs the ultimate quantity of carbon deposition on the surface of the oxygen carrier material.

As observed from the data presented in Fig. 11b, the total CO yield likewise demonstrates fundamental stability across multiple cycles,

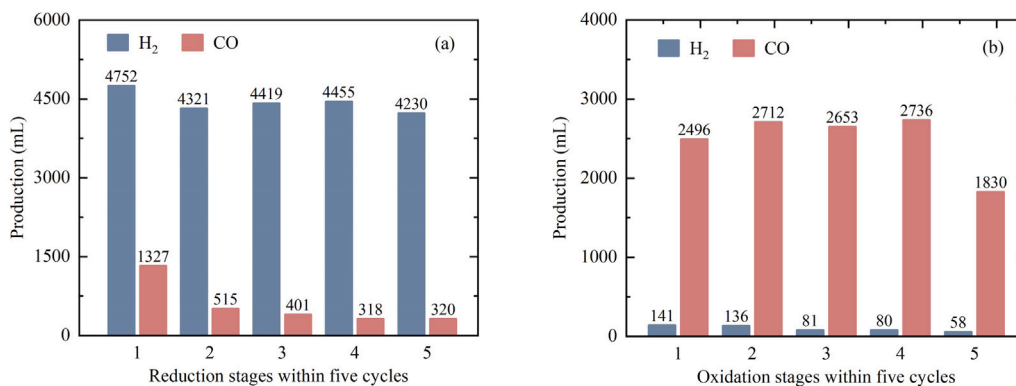


Fig. 11. Syngas production in (a) reduction stages and (b) oxidation stages within five cycles of the CL-DRM process.

with a conspicuous decline becoming apparent solely in the final cycle. Based on an assessment of the initial four cycles, it becomes apparent that the predominant factor contributing to this phenomenon is more directly linked to the omission of the reheating process during the fifth cycle, rather than the activation of oxygen carriers. The average CO production over the five cycles exceeded 2 L, maintaining an approximate 1:2 relationship with the H₂ production attained in the reduction stage. Additionally, a minimal amount of H₂ was generated in the oxidation stage, presumably from a portion of the H₂ that remained in the reactor chamber after the reduction stage. As the increase of cycling times, this part of H₂ tends to be completely eliminated. Overall, the experimental findings for both the oxidation and reduction stages validate that the CL-DRM reaction system effectively accomplishes an in-situ separation of fuel gas at each stage. This obviates the necessity for an auxiliary gas separation unit, which appears to constitute a significant advantage compared to the methane reforming reaction system. On the other hand, the CL-DRM enables considerable amounts of H₂ and CO production in the reduction stage, thus eliminating the disadvantage of the TSTC process which hardly produces value-added fuels in the reduction stage.

Further, Fig. 12 demonstrates the solar-to-fuel conversion efficiency over the course of five cycles. Given that CH₄ inherently possesses combustible properties characterized by a high calorific value, this study computed two distinct efficiency metrics: the solar-to-fuel conversion efficiency without accounting for the calorific value of CH₄, denoted as $\eta_{\text{solar-to-fuel}}$, and the net solar-to-fuel conversion efficiency after deducting the calorific value of CH₄, represented as $\eta_{\text{solar-to-fuel, net}}$. In addition to its role in enhancing the reactivity of oxygen carriers, the introduction of CH₄ auxiliary gas offers the feasibility of maintaining a real-time net conversion efficiency consistently above zero. This signifies that the contribution of CH₄ to energy efficiency consistently surpasses its inherent calorific value from direct combustion. Hence, from the perspective of energy conversion, the incorporation of CH₄ auxiliary gas is deemed advantageous for the two-step thermochemical reaction system. Under the current reaction conditions, the average solar-to-fuel conversion efficiency of the reaction process attains 2.80%, with a net efficiency of 1.93%. In terms of energy efficiency, the prepared FSM demonstrated a robust performance with negligible degradation during the nearly 6-hour experimental duration.

Furthermore, Table 4 provides a comparative analysis of the key experimental parameters between the CL-DRM and TSTC reaction processes, both conducted on the same experimental platform and employing identical FSM [67,68]. As previously noted, it is important to refrain from direct comparisons with a strictly solar-driven TSTC process, given the incorporation of reprocessed fossil fuels (CH₄) in the CL-DRM approach. Nevertheless, considering CL-DRM as one of the most promising carbon recovery technologies in the current landscape of high-temperature thermochemistry for potential large-scale industrialization, the primary emphasis here is placed exclusively on discerning

the distinctions between CL-DRM and TSTC processes with regard to reaction performance and application feasibility. An evident advantage lies in the fact that the CL-DRM reaction system, operating within a lower temperature range of 800 to 1200 K, demonstrates superior engineering potential owing to reduced heat loss and the alleviation of issues associated with high-temperature sintering. Regarding gas products, the limited quantity of oxygen generated by the TSTC process holds minimal economic significance, while the CO yield and overall production in the oxidation stage remain at a low level, primarily due to the high-temperature deactivation of the oxygen carrier. In contrast, the CL-DRM system exhibits the capability to produce a substantial amount of hydrogen product while increasing the single-cycle CO production by nearly 300%, thus allowing the final energy conversion efficiency to be more than doubled compared to the TSTC process. Additionally, a reasonable optimization of the process enables the in-situ separation of H₂ and CO from the syngas product, thus eliminating the additional energy consumption. One noteworthy point is that, in this study, the primary constraint on energy efficiency lies in the size of the reactor, as opposed to the reaction system and oxygen carrier. This argument has been substantiated in our previous works [68], suggesting that the current efficiency of 1.93% holds great potential for improvement through reactor upscaling. As a consequence, the iron-based CL-DRM reaction system is certainly appropriate as a critical pathway to achieving the industrial thermal reduction of CO₂ to solar fuels, or as an essential transition to maturity for direct thermal reduction of CO₂ without additional hydrogen sources. Additionally, it should be noted that the syngas yield per unit mass of the reaction materials developed in this study has reached a high level, while the required reaction temperature is relatively low, compared to some successful demonstration applications [16,17,32]. That is, a key limiting factor for the energy efficiency of the current system lies not in the reaction characteristics of the materials, but more significantly in the amount of material used, or in other words, the scale of the reactor [75]. Accordingly, subsequent research should focus on determining the optimal reactor volume based on the material properties, in order to enhance the potential for large-scale applications.

5. Conclusion

Focusing on the solar-driven iron-based CL-DRM process, this study undertakes pertinent numerical and experimental investigations. The primary objective is to unveil the intricate reaction mechanism, with a specific focus on reaction kinetics, while simultaneously achieving a comprehensive experimental validation and evaluation, spanning from the preparation of oxygen carriers to the practical application of the system. The main conclusions are as follows.

(1) A comprehensive reaction kinetic model for the CL-DRM process was developed by integrating the GRI-Mech 3.0 gas-phase reaction mechanism with kinetic data related to ferrite surface reactions. This

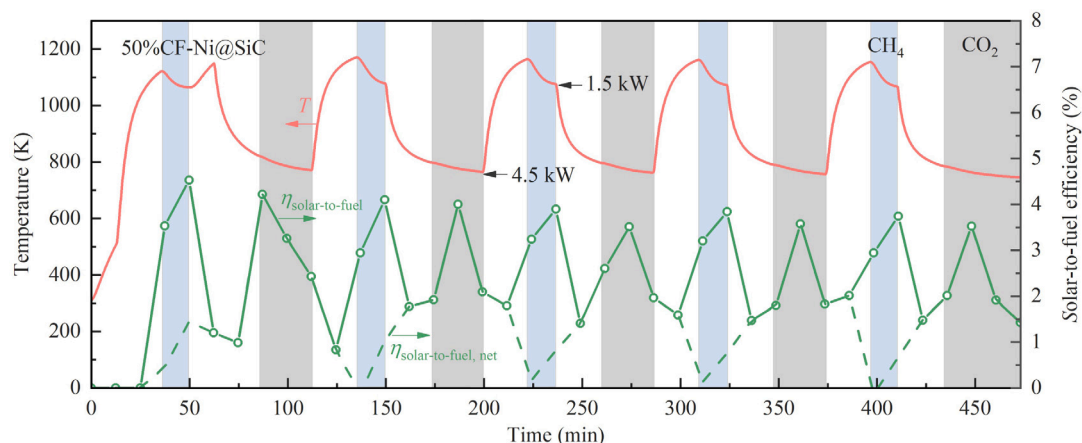


Fig. 12. Solar-to-fuel efficiency (refer to the right axis) under five cycles of the CL-DRM process.

Table 4
Comparison of key indicators of the TSTC and CL-DRM processes.

Item	TSTC [67,68]	CL-DRM
Feed gas	CO ₂	CH ₄ , CO ₂
Product	O ₂ , CO	H ₂ , CO
Reaction temperature (K)	1000–1600	800–1200
Peak H ₂ yield (mL.min ⁻¹ g ⁻¹)	0.0	23.5
Peak CO yield (mL.min ⁻¹ g ⁻¹)	7.0	11.6
Peak CH ₄ conversion (%)	–	89.6
Peak CO ₂ conversion (%)	22.8	46.1
H ₂ production in a single cycle (L)	0.0	4.8
CO production in a single cycle (L)	0.69	2.7
Thermal efficiency (%)	42	51
Net solar-to-fuel efficiency (%)	0.89	1.93

model is capable of delineating the detailed reaction pathways of reactants, uncovering the kinetic mechanisms governing reaction behavior, and subsequently providing a numerical reference for determining optimal reaction conditions. Moreover, it offers the flexibility to incorporate new reactions and their associated kinetic data, thereby serving as a foundation for modeling the reaction kinetics of alternative iron-based oxygen carriers.

(2) Given the pronounced reactivity of Fe towards CO₂ and Ni towards CH₄, oxygen carriers comprising 50wt% NiO-doped CoFe₂O₄ were synthesized, and subsequently integrated with SiC ceramic foams to prepare foam-structured materials. The development of this material allowed for practical experiments, and the corresponding outcomes underscored the exceptional reaction performance of the Ni–Fe bi-activated metal oxygen carriers within the CL-DRM reaction system. At reaction temperatures below 1200 K, the peak H₂ and CO yields reached 23.5 mL.min⁻¹ g⁻¹ and 11.6 mL.min⁻¹ g⁻¹, while the total H₂ and CO production within a single cycle was up to 4.8 L and 2.7 L, respectively.

(3) Systematic experimental validation and evaluation were conducted using a self-designed solar thermochemistry experimental platform, so as to provide prospective references for the eventual industrial implementation of the CL-DRM process. Under the current operating conditions, the calculated steady-state thermal efficiency stands at approximately 51%, accompanied by a net solar-to-fuel conversion efficiency of 1.93%. The potential for substantial improvement in this energy efficiency should be clarified, given its noteworthy constraints associated with the reactor volume and the utilization of oxygen carriers. Furthermore, comparative experiments employing identical reaction materials within the same experimental setup demonstrated that the syngas production and energy efficiency of the CL-DRM were consistently double that of the TSTC process. Consequently, within the present technological framework, CL-DRM emerges

as a more promising candidate for large-scale engineering applications, alternatively, serving as an essential bridge to the maturity of the TSTC reaction system.

On the numerical front, future research endeavors will center on refining the developed reaction kinetic model, including augmenting the comprehensive carbon deposition mechanism. Concurrently, on the experimental side, efforts will be directed towards optimizing the solar reactor to enhance the validation experiments for the entire solar thermochemical system. Besides, delving into the quantification of solar energy absorption and conversion at each stage of the physical and chemical processes, with a focus on energy utilization, appears to be a compelling area of exploration.

CRediT authorship contribution statement

Hao Zhang: Writing – original draft, Software, Methodology, Investigation, Funding acquisition, Conceptualization. **Dazhi Yang:** Writing – review & editing, Validation, Supervision, Funding acquisition. **Yong Shuai:** Writing – review & editing, Supervision, Project administration. **Xiaomi Zhang:** Writing – original draft, Supervision, Resources, Investigation. **Boxi Geng:** Visualization, Validation, Data curation. **Boshu Jiang:** Investigation, Resources, Validation. **Bachirou Guene Lougou:** Resources, Investigation, Formal analysis. **Dongmei Han:** Validation, Software, Investigation. **Qinghui Pan:** Resources, Funding acquisition. **Fuqiang Wang:** Writing – review & editing, Resources.

Declaration of competing interest

The authors declare that they have no known competing financial interests or personal relationships that could have appeared to influence the work reported in this paper.

Data availability

Data will be made available on request.

Acknowledgments

This work was supported by China Postdoctoral Science Foundation [2023M740908], Heilongjiang Postdoctoral Fund, China [LBH-Z22120], Heilongjiang Provincial Education Department Research Fund [LJYXL2022-061], and Fundamental Research Funds for the Central Universities, China [2022ZFJH04].

References

- [1] A.I. Osman, M. Hefny, M.I.A. Abdel Maksoud, A.M. Elgarahy, D.W. Rooney, Recent advances in carbon capture storage and utilisation technologies: A review, *Environ. Chem. Lett.* 19 (2) (2021) 797–849, <http://dx.doi.org/10.1007/s10311-020-01133-3>.
- [2] H. Song, S. Luo, H. Huang, B. Deng, J. Ye, Solar-driven hydrogen production: Recent advances, challenges, and future perspectives, *ACS Energy Lett.* 7 (3) (2022) 1043–1065, <http://dx.doi.org/10.1021/acseenergylett.1c02591>.
- [3] Z. Dong, C. Xia, K. Fang, W. Zhang, Effect of the carbon emissions trading policy on the co-benefits of carbon emissions reduction and air pollution control, *Energy Policy* 165 (2022) <http://dx.doi.org/10.1016/j.enpol.2022.112998>.
- [4] A. Mustafa, B.G. Lougou, Y. Shuai, Z. Wang, H. Tan, Current technology development for CO₂ utilization into solar fuels and chemicals: A review, *J. Energy Chem.* 49 (2020) 96–123, <http://dx.doi.org/10.1016/j.jechem.2020.01.023>.
- [5] R. Pan, G. Debenest, Numerical investigation of a novel smoldering-driven reactor for plastic waste pyrolysis, *Energy Convers. Manage.* 257 (2022) 115439, <http://dx.doi.org/10.1016/j.enconman.2022.115439>.
- [6] D. Yadav, R. Banerjee, A review of solar thermochemical processes, *Renew. Sustain. Energy Rev.* 54 (2016) 497–532, <http://dx.doi.org/10.1016/j.rser.2015.10.026>.
- [7] A.M. Ranjekar, G.D. Yadav, Dry reforming of methane for syngas production: A review and assessment of catalyst development and efficacy, *J. Indian Chem. Soc.* 98 (1) (2021) 100002, <http://dx.doi.org/10.1016/j.jics.2021.100002>.
- [8] F. Safari, I. Dincer, A review and comparative evaluation of thermochemical water splitting cycles for hydrogen production, *Energy Convers. Manage.* 205 (2020) 112182, <http://dx.doi.org/10.1016/j.enconman.2019.112182>.
- [9] M. Najera, R. Solunke, T. Gardner, G. Vesper, Carbon capture and utilization via chemical looping dry reforming, *Chem. Eng. Res. Des.* 89 (9) (2011) 1533–1543, <http://dx.doi.org/10.1016/j.cherd.2010.12.017>.
- [10] L.-S. Fan, Introduction, in: *Chemical looping systems for fossil energy conversions*, John Wiley & Sons, Ltd, 2010, pp. 1–56, <http://dx.doi.org/10.1002/9780470872888.ch1>.
- [11] L.-S. Fan, Overview, in: *Chemical looping partial oxidation: Gasification, reforming, and chemical syntheses*, in: Cambridge Series in Chemical Engineering, Cambridge University Press, 2017, pp. 1–54, <http://dx.doi.org/10.1017/9781108157841.002>.
- [12] F. Jiao, T. Liu, C. Chen, B. Lu, Y. Long, Q. Liu, Advances in solar thermochemical cycles for hydrogen production, *Chin. Sci. Bull. Chin.* 67 (19) (2022) 2142–2157, <http://dx.doi.org/10.1360/TB-2022-0105>.
- [13] J.E. Lee, I. Shafiq, M. Hussain, S.S. Lam, G.H. Rhee, Y.-K. Park, A review on integrated thermochemical hydrogen production from water, *Int. J. Hydrog. Energy* 47 (7) (2022) 4346–4356, <http://dx.doi.org/10.1016/j.ijhydene.2021.11.065>.
- [14] Z. Alipour, V. Babu Borugadda, H. Wang, A.K. Dalai, Syngas production through dry reforming: A review on catalysts and their materials, preparation methods and reactor type, *Chem. Eng. J.* 452 (2023) 139416, <http://dx.doi.org/10.1016/j.cej.2022.139416>.
- [15] G. Yang, D. Yang, M.J. Perez, R. Perez, J. Kleissl, J. Remund, M. Pierro, Y. Cheng, Y. Wang, X. Xia, J. Xu, C. Lyu, B. Liu, H. Zhang, Hydrogen production using curtailed electricity of firm photovoltaic plants: Conception, modeling, and optimization, *Energy Convers. Manage.* 308 (2024) 118356, <http://dx.doi.org/10.1016/j.enconman.2024.118356>.
- [16] D. Marxer, P. Furler, M. Takacs, A. Steinfeld, Solar thermochemical splitting of CO₂ into separate streams of CO and O₂ with high selectivity, stability, conversion, and efficiency, *Energy Environ. Sci.* 10 (2017) 1142–1149, <http://dx.doi.org/10.1039/C6EE03776C>.
- [17] R. Schüppli, D. Rutz, F. Dähler, A. Muroyama, P. Haueter, J. Lilliestam, A. Patt, P. Furler, A. Steinfeld, Drop-in fuels from sunlight and air, *Nature* 601 (7891) (2022) 63+, <http://dx.doi.org/10.1038/s41586-021-04174-y>.
- [18] Y. Mao, Y. Gao, W. Dong, H. Wu, Z. Song, X. Zhao, J. Sun, W. Wang, Hydrogen production via a two-step water splitting thermochemical cycle based on metal oxide - A review, *Appl. Energy* 267 (2020) 114860, <http://dx.doi.org/10.1016/j.apenergy.2020.114860>.
- [19] D. Li, R. Xu, Z. Gu, X. Zhu, S. Qing, K. Li, Chemical-looping conversion of methane: A review, *Energy Technol.* 8 (8) (2020) 1900925, <http://dx.doi.org/10.1002/ente.201900925>.
- [20] M. Tang, L. Xu, M. Fan, Progress in oxygen carrier development of methane-based chemical-looping reforming: A review, *Appl. Energy* 151 (2015) 143–156, <http://dx.doi.org/10.1016/j.apenergy.2015.04.017>.
- [21] F. Jin, C. Xu, H. Yu, X. Xia, F. Ye, X. Li, X. Du, Y. Yang, CaCo_{0.05}Mn_{0.95}O_{3-δ}: A promising perovskite solid solution for solar thermochemical energy storage, *ACS Appl. Mater. Interfaces* 13 (3) (2021) 3856–3866, <http://dx.doi.org/10.1021/acsaami.0c18207>.
- [22] D. Li, R. Xu, X. Li, Z. Li, X. Zhu, K. Li, Chemical looping conversion of gaseous and liquid fuels for chemical production: A review, *Energy Fuels* 34 (5) (2020) 5381–5413, <http://dx.doi.org/10.1021/acs.energyfuels.0c01006>.
- [23] A. Riaz, M.U. Ali, T.G. Enge, T. Tsuzuki, A. Lowe, W. Lipiński, Concentration-dependent solar thermochemical CO₂/H₂O splitting performance by vanadia-ceria multiphase metal oxide systems, *Research* 2020 (2020) 3049534, <http://dx.doi.org/10.34133/2020/3049534>.
- [24] V.K. Budama, J.P.R. Duarte, M. Roeb, C. Sattler, Potential of solar thermochemical water-splitting cycles: A review, *Sol. Energy* 249 (2023) 353–366, <http://dx.doi.org/10.1016/j.solener.2022.11.001>.
- [25] S. Bellan, T. Kodama, N. Gokon, K. Matsubara, A review on high-temperature thermochemical heat storage: Particle reactors and materials based on solid-gas reactions, *WIREs Energy Environ.* 11 (5) (2022) e440, <http://dx.doi.org/10.1002/wene.440>.
- [26] F. Jin, C. Xu, J. King, X. Li, X. Xia, Z. Liao, Thermodynamic analysis of titanium dioxide-based isothermal methanothermal and carbothermal redox cycles for solar fuel production, *Energy Convers. Manage.* 254 (2022) 115254, <http://dx.doi.org/10.1016/j.enconman.2022.115254>.
- [27] M. Fu, T. Ma, L. Wang, S. Dai, Z. Chang, H. Xu, J. Liu, X. Li, Hydrogen production via a novel two-step solar thermochemical cycle based on non-volatile GeO₂, *Sol. Energy* 179 (2019) 30–36, <http://dx.doi.org/10.1016/j.solener.2018.12.050>.
- [28] M. Fu, H. Xu, H. Ma, X. Li, Theoretical assessment of hydrogen production and multicycle energy conversion via solar thermochemical cycle based on nonvolatile SnO₂, *J. Energy Chem.* 38 (2019) 177–184, <http://dx.doi.org/10.1016/j.jechem.2019.03.035>.
- [29] K.J. Warren, J.R. Scheffe, Role of surface oxygen vacancy concentration on the dissociation of methane over nonstoichiometric ceria, *J. Phys. Chem. C* 123 (21) (2019) 13208–13218, <http://dx.doi.org/10.1021/acs.jpcc.9b01352>.
- [30] Z. Zhao, M. Uddi, N. Tsvetkov, B. Yildiz, A.F. Ghoniem, Redox kinetics study of fuel reduced ceria for chemical-looping water splitting, *J. Phys. Chem. C* 120 (30) (2016) 16271–16289, <http://dx.doi.org/10.1021/acs.jpcc.6b01847>.
- [31] A. Riaz, F. Kremer, T. Kim, S. Sattayaporn, T. Tsuzuki, W. Lipiński, A. Lowe, Experimental demonstration of vanadium-doped nanostructured ceria for enhanced solar thermochemical syngas production, *Nano Energy* 81 (2021) 105639, <http://dx.doi.org/10.1016/j.nanoen.2020.105639>.
- [32] M. Zuber, M. Patriarca, S. Ackermann, P. Furler, R. Conceição, J. Gonzalez-Aguilar, M. Romero, A. Steinfeld, Methane dry reforming via a ceria-based redox cycle in a concentrating solar tower, *Sustain. Energy Fuels* 7 (2023) 1804–1817, <http://dx.doi.org/10.1039/D2SE01726A>.
- [33] A. Riaz, C.I. Bodger, J. Chen, A. Lowe, T. Tsuzuki, W. Lipiński, Redox performance of ceria–vanadia mixed-phase reticulated porous ceramics for solar thermochemical syngas production, *Energy Fuels* 35 (20) (2021) 16791–16798, <http://dx.doi.org/10.1021/acs.energyfuels.1c01856>.
- [34] C. Huang, J. Wu, Y.-T. Chen, M. Tian, A.I. Rykov, B. Hou, J. Lin, C.-R. Chang, X. Pan, J. Wang, A. Wang, X. Wang, In situ encapsulation of iron(0) for solar thermochemical syngas production over iron-based perovskite material, *Commun. Chem.* 1 (2018) <http://dx.doi.org/10.1038/s42004-018-0050-y>.
- [35] A. Steinfeld, P. Kuhn, J. Karni, High-temperature solar thermochemistry: Production of iron and synthesis gas by Fe₃O₄-reduction with methane, *Energy* 18 (3) (1993) 239–249, [http://dx.doi.org/10.1016/0360-5442\(93\)90108-P](http://dx.doi.org/10.1016/0360-5442(93)90108-P).
- [36] Y. Kang, Y. Han, C. Wei, K. Liu, M. Tian, C. Huang, C. Wang, J. Lin, B. Hou, X. Pan, Y. Su, L. Li, R. Zhang, Y. Hao, X. Wang, A novel carbon cycle process assisted by Ni/La₂O₃ catalyst for enhanced thermochemical CO₂ splitting, *J. Energy Chem.* 61 (2021) 297–303, <http://dx.doi.org/10.1016/j.jechem.2021.03.026>.
- [37] T. Kodama, T. Shimizu, T. Satoh, M. Nakata, K.-I. Shimizu, Stepwise production of CO-rich syngas and hydrogen via solar methane reforming by using a Ni(II)-ferrite redox system, *Sol. Energy* 73 (5) (2002) 363–374, [http://dx.doi.org/10.1016/S0038-092X\(02\)00112-3](http://dx.doi.org/10.1016/S0038-092X(02)00112-3).
- [38] Y. Hu, J. Wu, Y. Han, W. Xu, L. Zhang, X. Xia, C. Huang, Y. Zhu, M. Tian, Y. Su, L. Li, B. Hou, J. Lin, W. Liu, X. Wang, Intensified solar thermochemical CO₂ splitting over iron-based redox materials via perovskite-mediated dealloying-exsolution cycles, *Chin. J. Catal.* 42 (11) (2021) 2049–2058, [http://dx.doi.org/10.1016/S1872-2067\(21\)63857-3](http://dx.doi.org/10.1016/S1872-2067(21)63857-3).
- [39] F. Wang, X. Zhang, Y. Dong, H. Yi, S. Xuhang, Y. Li, Z. Cheng, Progress in radiative transfer in porous medium: A review from macro scale to pore scale with experimental test, *Appl. Therm. Eng.* 210 (2022) 118331, <http://dx.doi.org/10.1016/j.applthermaleng.2022.118331>.
- [40] J.R. Fosheim, B.J. Hathaway, J.H. Davidson, High efficiency solar chemical-looping methane reforming with ceria in a fixed-bed reactor, *Energy* 169 (2019) 597–612, <http://dx.doi.org/10.1016/j.energy.2018.12.037>.
- [41] B. Bulfin, S. Ackermann, P. Furler, A. Steinfeld, Thermodynamic comparison of solar methane reforming via catalytic and redox cycle routes, *Sol. Energy* 215 (2021) 169–178, <http://dx.doi.org/10.1016/j.solener.2020.11.076>.
- [42] S. Chuayboon, S. Abanades, S. Rodat, Syngas production via solar-driven chemical looping methane reforming from redox cycling of ceria porous foam in a volumetric solar reactor, *Chem. Eng. J.* 356 (2019) 756–770, <http://dx.doi.org/10.1016/j.cej.2018.09.072>.
- [43] K.J. Warren, R.J. Carrillo, B. Greek, C.M. Hill, J.R. Scheffe, Solar reactor demonstration of efficient and selective syngas production via chemical-looping dry reforming of methane over ceria, *Energy Technol.* 8 (6) (2020) 2000053, <http://dx.doi.org/10.1002/ente.202000053>.

- [44] F. Wang, G. Zhang, X. Shi, Y. Dong, Y. Xun, A. Zhang, Biomimetically calabash-inspired phase change material capsule: Experimental and numerical analysis on thermal performance and flow characteristics, *J. Energy Storage* 52 (2022) 104859, <http://dx.doi.org/10.1016/j.est.2022.104859>.
- [45] L. Wang, T. Ma, Z. Chang, H. Li, M. Fu, X. Li, Solar fuels production via two-step thermochemical cycle based on $\text{Fe}_3\text{O}_4/\text{Fe}$ with methane reduction, *Sol. Energy* 177 (2019) 772–781, <http://dx.doi.org/10.1016/j.solener.2018.12.009>.
- [46] E.R. Monazam, R.W. Breault, R. Siriwardane, G. Richards, S. Carpenter, Kinetics of the reduction of hematite (Fe_2O_3) by methane (CH_4) during chemical looping combustion: A global mechanism, *Chem. Eng. J.* 232 (2013) 478–487, <http://dx.doi.org/10.1016/j.cej.2013.07.091>.
- [47] G.P. Smith, D.M. Golden, M. Frenklach, N.W. Moriarty, B. Eiteneer, M. Goldenberg, C.T. Bowman, R.K. Hanson, S. Song, W.C. Gardiner Jr., V.V. Lissianski, Z. Qin, GRI-Mech 3.0 reaction mechanism, 2023, https://www.me.berkeley.edu/gri_mech/.
- [48] Ansys Inc, Chemkin documentation of ANSYS Chemkin 17.0 software package, 2016.
- [49] N. Ren, F. Wang, J. Zhang, X. Zheng, Progress in thermal analysis kinetics, *Acta Phys.-Chim. Sin.* 36 (6) (2020) <http://dx.doi.org/10.3866/PKU.WHXB201905062>.
- [50] A. Burcat, Burcat's thermodynamic data, 2023, <http://garfield.chem.elte.hu/Burcat/burcat.html>.
- [51] H.E. Bush, P.G. Loutzenhiser, Solar electricity via an Air Brayton cycle with an integrated two-step thermochemical cycle for heat storage based on $\text{Fe}_2\text{O}_3/\text{Fe}_3\text{O}_4$ redox reactions: Thermodynamic and kinetic analyses, *Sol. Energy* 174 (2018) 617–627, <http://dx.doi.org/10.1016/j.solener.2018.09.043>.
- [52] A. Abad, J. Adánez, F. García-Labiano, L.F. de Diego, P. Gayán, J. Celaya, Mapping of the range of operational conditions for Cu-, Fe-, and Ni-based oxygen carriers in chemical-looping combustion, *Chem. Eng. Sci.* 62 (1) (2007) 533–549, <http://dx.doi.org/10.1016/j.ces.2006.09.019>.
- [53] K.-S. Kang, C.-H. Kim, K.-K. Bae, W.-C. Cho, S.-U. Jeong, Y.-J. Lee, C.-S. Park, Reduction and oxidation properties of $\text{Fe}_2\text{O}_3/\text{ZrO}_2$ oxygen carrier for hydrogen production, *Chem. Eng. Res. Des.* 92 (11) (2014) 2584–2597, <http://dx.doi.org/10.1016/j.cherd.2014.04.001>.
- [54] R. Xu, T.F. Wiesner, Conceptual design of a two-step solar hydrogen thermochemical cycle with thermal storage in a reaction intermediate, *Int. J. Hydrog. Energy* 39 (24) (2014) 12457–12471, <http://dx.doi.org/10.1016/j.ijhydene.2014.06.064>.
- [55] L.C. Buelens, V.V. Galvita, H. Poelman, C. Detavernier, G.B. Marin, Kinetics of multi-step redox processes by time-resolved in situ X-ray diffraction, *Chem. Ing. Tech.* 88 (11) (2016) 1684–1692, <http://dx.doi.org/10.1002/cite.201600057>.
- [56] J. Zhu, W. Wang, S. Lian, X. Hua, Z. Xia, Stepwise reduction kinetics of iron-based oxygen carriers by CO/CO_2 mixture gases for chemical looping hydrogen generation, *J. Mater. Cycles Waste Manag.* 19 (1) (2017) 453–462, <http://dx.doi.org/10.1007/s10163-015-0443-2>.
- [57] M.H. Jeong, D.H. Lee, G.Y. Han, C.-H. Shin, M.K. Shin, C.K. Ko, J.W. Bae, Reduction-oxidation kinetics of three different iron oxide phases for CO_2 activation to CO, *Fuel* 202 (2017) 547–555, <http://dx.doi.org/10.1016/j.fuel.2017.04.076>.
- [58] National institute of standards and technology, NIST chemical kinetics database, 2023, <https://kinetics.nist.gov/kinetics/index.jsp>.
- [59] P. Loutzenhiser, M. Gálvez, I. Hischer, A. Stamatou, A. Frei, A. Steinfeld, CO_2 splitting via two-step solar thermochemical cycles with Zn/ZnO and $\text{FeO}/\text{Fe}_3\text{O}_4$ redox reactions II: kinetic analysis, *Energy Fuels* 23 (5) (2009) 2832–2839, <http://dx.doi.org/10.1021/ef801142b>.
- [60] Z. Liu, L. Yang, E. Song, J. Wang, A. Zare, T.A. Bodisco, R.J. Brown, Development of a reduced multi-component combustion mechanism for a diesel/natural gas dual fuel engine by cross-reaction analysis, *Fuel* 293 (2021) 120388, <http://dx.doi.org/10.1016/j.fuel.2021.120388>.
- [61] T. Lu, C.K. Law, A directed relation graph method for mechanism reduction, *Proc. Combust. Inst.* 30 (1) (2005) 1333–1341, <http://dx.doi.org/10.1016/j.proci.2004.08.145>.
- [62] H. Zhang, B. Guene Lougou, R. Pan, Y. Shuai, F. Wang, Z. Cheng, H. Tan, Analysis of thermal transport and fluid flow in high-temperature porous media solar thermochemical reactor, *Sol. Energy* 173 (2018) 814–824, <http://dx.doi.org/10.1016/j.solener.2018.08.015>.
- [63] S. Yang, W. Tao, *Heat Transfer*, fourth ed., Higher Education Press, Beijing, 2006, p. 8.
- [64] H. Zhang, Y. Shuai, B.G. Lougou, B. Jiang, D. Yang, Q. Pan, F. Wang, X. Huang, Effects of foam structure on thermochemical characteristics of porous-filled solar reactor, *Energy* 239 (2022) 122219, <http://dx.doi.org/10.1016/j.energy.2021.122219>.
- [65] L. Wu, B. Guene Lougou, B. Jiang, H. Zhang, Y. Guo, B. Geng, T. Yan, P. Lapka, Y. Shuai, Experimentally validated numerical model of multi-spectral bands radiative transport in solar receiver/reactor with photo-active porous absorber reacting media, *Energy Convers. Manage.* 278 (2023) 116740, <http://dx.doi.org/10.1016/j.enconman.2023.116740>.
- [66] H. Zhang, Y. Shuai, Y. Yuan, B. Guene Lougou, B. Jiang, F. Wang, Z. Cheng, Thermal-chemical reaction characteristics of $\text{Ni}/\text{Al}_2\text{O}_3$ catalytic porous material filled solar reactor for dry reforming of methane process, *Appl. Therm. Eng.* 180 (2020) 115901, <http://dx.doi.org/10.1016/j.applthermaleng.2020.115901>.
- [67] H. Zhang, X. Zhang, D. Yang, Y. Shuai, B.G. Lougou, Q. Pan, F. Wang, Selection of iron-based oxygen carriers for two-step solar thermochemical splitting of carbon dioxide, *Energy Convers. Manage.* 279 (2023) 116772, <http://dx.doi.org/10.1016/j.enconman.2023.116772>.
- [68] H. Zhang, X. Zhang, D. Yang, Y. Shuai, B.G. Lougou, Q. Pan, F. Wang, Application of CoFe_2O_4 - NiO nanoparticle-coated foam-structured material in a high-flux solar thermochemical reactor, *Sci. China Technol. Sci.* 66 (2023) <http://dx.doi.org/10.1007/s11431-023-2397-7>.
- [69] H. Zhang, Y. Shuai, S. Pang, R. Pan, B.G. Lougou, X. Huang, Numerical investigation of carbon deposition behavior in $\text{Ni}/\text{Al}_2\text{O}_3$ -based catalyst porous-filled solar thermochemical reactor for the dry reforming of methane process, *Ind. Eng. Chem. Res.* 58 (34) (2019) 15701–15711, <http://dx.doi.org/10.1021/acs.iecr.9b02486>.
- [70] A. Steinfeld, A. Frei, P. Kuhn, Thermoanalysis of the combined Fe_3O_4 -reduction and CH_4 -reforming processes, *Metall. Mater. Trans. B* 26 (3) (1995) 509–515, <http://dx.doi.org/10.1007/BF02653867>.
- [71] F. Li, L. Zeng, S. Ramkumar, D. Sridhar, M. Iyer, L.-S. Fan, Chemical looping gasification using gaseous fuels, in: *Chemical looping systems for fossil energy conversions*, John Wiley & Sons, Ltd, 2010, pp. 215–300, <http://dx.doi.org/10.1002/9780470872888.ch4>.
- [72] L.-S. Fan, Metal oxide oxygen carriers, in: *Chemical looping partial oxidation: Gasification, reforming, and chemical syntheses*, in: Cambridge Series in Chemical Engineering, Cambridge University Press, 2017, pp. 55–171, <http://dx.doi.org/10.1017/9781108157841.003>.
- [73] H. Zhang, X. Zhang, D. Yang, B. Liu, Y. Shuai, B.G. Lougou, Q. Zhou, X. Huang, F. Wang, Comparison of non-isothermal and isothermal cycles in a novel methane-assisted two-step thermochemical process, *Renew. Energy* 230 (2024) 120817, <http://dx.doi.org/10.1016/j.renene.2024.120817>.
- [74] B. Jiang, Q. Sun, B. Guene Lougou, H. Zhang, X. Li, Z. Qu, Y. Shuai, C.-H. Wang, Highly-selective CO_2 conversion through single oxide CuO -enhanced NiFe_2O_4 thermal catalytic activity, *Sustain. Mater. Technol.* 32 (2022) e00441, <http://dx.doi.org/10.1016/j.susmat.2022.e00441>.
- [75] W.C. Chueh, C. Falter, M. Abbott, D. Scipio, P. Furler, S.M. Haile, A. Steinfeld, High-flux solar-driven thermochemical dissociation of CO_2 and H_2O using non-stoichiometric ceria, *Science* 330 (6012) (2010) 1797–1801, <http://dx.doi.org/10.1126/science.1197834>.